הטכניון
מכון טכנולוגי לישראל
TECHNION
Israel Institute of Technology

ספריות הטכניון
The Technion Libraries

בית הספר ללימודי מוסמכים ע"ש ארווין וג'ואן ג'ייקובס
Irwin and Joan Jacobs Graduate School

Turbulence of Anabatic (Up-Slope) Thermally Driven Flow

Research Thesis in Partial Fulfilment of the Requirements for the Degree of Master of Science in Environmental Quality Sciences (with thesis)

Roni Hilel

Submitted to the Senate of the Technion - Israel Institute of Technology

Elul, 5776 Haifa, September, 2016

The research thesis was completed under the supervision of
Assistant Professor Dan Liberzon
in the Faculty of Civil and Environmental Engineering

The generous financial support of the
United States-Israel Binational Science Fund
(Grant 2014075) is gratefully acknowledged

ACKNOWLEDGEMENTS

I would like to give my most sincere thanks to my advisor Asst. Professor Dan Liberzon for introducing me to the wonders of scientific research. Dan, thank you for your guidance, patience, support, and for always having the door to your office open. Everyone knows how busy professors are (especially ones constructing a new lab) and I appreciate that you always make an effort for your students (I know that Uri and Almog agree!). My fellow T-SAIL lab mates, Almog Shani-Zerbib and Uri Itay, thank you for the hours of support and entertainment, the last two years would not have been the same without you two.

I gratefully acknowledge the support of this study by the United States – Israel Binational Science Foundation under Grant 2014075. I also thank Prof. H.J.S. Fernando of the University Of Notre Dame and Prof. David Broday of the Technion for lending us part of the equipment used in this study. A special thank you for the Richter-Baruch family for hosting us at their property with great hospitality and providing all possible support during the summer months of 2015.

My family, thank you for always reminding me that my job in life is to do what I love and for always believing in me. Ima, Aba, Amosy, and Yardeny! Thank you for all of your support every day! My life partner, Itay Goldshmid, thank you for always pushing me to continue with the path that I have chosen and for always being there for me. The extended family (Agrantys, Ben-Ezras, Dahans, Gadassis, Hilels, Vidals, Vidavskis, Yaakovs), thank you for being the best, most loving, and supporting family that you are here in Israel while my parents and siblings live on the other side of the planet.

Abstract

Understanding the physical nature of thermally driven upslope (anabatic) and downslope (katabatic) turbulent flows in the atmospheric-boundary layer is of paramount importance for producing accurate weather forecasts, investigating climate processes, and gaining a better understanding of pollution transport in complex terrains. Of particular interest are the microclimates of urban centers which are often positioned in valleys and next to mountain ridges. The large scales of turbulent flows may simply be measured with inexpensive low spatial and temporal resolution instrumentation such as the ultrasonic anemometers (Sonic), while fine scales are generally estimated using Kolmogorov's $-5/3$ theory due to measuring impediments such as the calibration of hot-wire/film anemometers. However, natural thermally driven turbulent flows are anisotropic and not homogeneous deducing that Kolmogorov's theory is not sufficient to describe such flows nor to be used as an extrapolation basis; nonetheless, these flows lack comprehensive models to describe them. These models are ought to include several statistical parameters such as turbulence intensity (TI), turbulent kinetic energy (TKE) dissipation rates, velocity derivative skewness, and various length scales with respect to *Re.* The length scales consist of Kolmogorov length scale (an indication of viscous forcing dominance), Taylor length (an indication of the size at which viscous forcing begins to play a role in the cascade of TKE dissipation), and horizontal length scale (an indication of the size of eddies in which the energy input occurs). Eventually, the fully resolved spectra of all three-velocity field components is required in order to characterize the behavior of the turbulent flow. Furthermore, the often-present phenomenon of short-timed rapid increase in velocity fluctuations intensity, bursting, is virtually impossible to capture in natural setups with low spatial-temporal instrumentation, yet it plays an important role in setting the turbulent flow energy cascade. Therefore, in addressing the need for high accuracy data on the turbulent statistics of anabatic flows, a field experiment was staged to obtain continuous high accuracy measurements of the diurnal cycle of thermally driven flow over moderate slope. The main instrument allowing high-resolution measurements of the velocity field in interest was a recently developed collocated Sonic and hot-film (HF) anemometer—Combo probe. In this instrument, the simultaneously measured slow data from the Sonic is used for *in-situ* calibration of the HF voltages using Neural Networks. This allowed investigation of both mean and fluctuating

components of the upslope flow, and additional instruments were used to record temperature fluctuations at two heights effectively detecting periods of stable and unstable stratification of the air mass on the slope. Strong correlation of the developing flow with the diurnal heating was detected in absence of significant synoptic forcing. Detailed analysis of turbulence statistics is provided; the main products being the fully resolved spectra of all three velocity field components, various turbulence statistics, characterization of the bursting phenomenon (i.e. length scales, frequency of appearance of bursting, and examination of the generation mechanism), comparison of and the flow's characterizing length scales (Kolmogorov, Taylor, and horizontal) in minutes including and excluding bursting, and empirical fits were made available for future measurements with low-resolution instruments and numerical models.

Contents

List of Figures

List of Tables

Nomenclature

Acronyms/Single Letters

BL	Boundary Layer
C	Universal Kolmogorov's constant
f	Frequency
k	Wave number
L	Sonic's smallest detectable eddy
HF	Hot film probes
NN	Neural Network
P	Power density of velocity fluctuations
Re	Reynolds number
Sk	Velocity derivative skewness
T	Temperature
t	Time
TFA	Taylor's Frozen Approximation
TI	Turbulence Intensity
TKE	Turbulent Kinetic Energy
u	Mean flow velocity
v	Horizontal orthogonal velocity component
w	Vertical orthogonal velocity component

Greek Symbols

∂	Partial derivative
α	Alignment angle
ΔT	Temperature difference
ε	TKE dissipation rate
η	Kolmogorov Length Scale
θ	Direction of the mean velocity (meteorological angle)
λ	Spatial resolution of the Sonic
ν	Kinematic viscosity

Other Symbols

$\sim$ (tilde)	Order of
$'$ (prime)	Fluctuations around mean value
$\bar{}$ (over line)	Average
°	Degrees
°C	Degrees Celsius

Subscripts

max	Maximum
min	Minimum
p	Probe's coordinate system
s	Sonic's coordinate system
u, v, w	Each component in probe's coordinate system

Chapter 1 Introduction

Turbulent flows are common everywhere in nature, they are readily visible to the human eye in smoke from chimneys and volcanos, waterfalls and rivers flows, and are often felt in airplanes while experiencing strong oscillations of winds. There are various scales of atmospheric turbulent flows ranging from the smaller scale such as cumulus clouds to mesoscales such as global transport of aerosols. Turbulent flows are frequently driven by thermal forces such as the solar heating cycle of earth surface or heat exchange with large bodies of water, and are therefore common in complex topography. Probably the most important are the thermally driven anabatic (up-slope) and katabatic (down-slope) flows developing on hills and slopes of mountains as these determine the in/out-fluxes of particles and gasses, ventilation, cloud formation, and precipitation regimes in the adjutant valleys. As more than 70 percent of world's cities are established in valleys surrounded by complex topography (Whiteman 1990) slope flows have a great impact on the daily human activities. Such flows develop due to the diurnal cycle of heating-cooling of the slopes' surfaces and when synoptic systems are weak these thermal circulations are dominant in determining the local climates.

The two main types of the slope flows, anabatic and katabatic, are very different in terms of generation mechanisms, turbulent characteristics, and eventually the impact on the surroundings. Anabatic flows are initiated by the diurnal heating of the slopes, mainly by solar radiation. In the morning, when the sun rises it warms up the slope's surface at much higher rate than the air above. Heat fluxed from the slope to the lower mass of the air causes temperature raise of the latter, eventually creating an unstable stratification of the air—warmer and lighter air is situated below the cooler and heavier air mass above. The resulted mixing initiates the upslope inclinations of the flow, eventually developing into a boundary layer flow up the slope characterized by high levels of turbulence. Another common mechanism for anabatic flows generation in cities surrounded by valleys is the heat island that occurs from daily human activities. The heat island is much warmer than the surrounding natural topography and generates anabatic flows. The rising flows carry large amount of air up the slope injecting it into the usually cooler and dryer air atop often triggering clouds formation, pollutants' transport and heat transfer rates will also be strongly affected by such flows. A major part of climate research is the investigation of atmospheric boundary-layer (BL) flows as they influence the transport of

contaminants endangering human health, heat transfer therein influences microclimates, and large eddies therein generate formation of clouds (Faller 1965; Ellis et al. 2000; Fernando et al. 2001; Otarola et al. 2016). Specifically, complex mountainous terrains and their topography complicate the local wind systems that are driven by thermal forces and appear as anabatic and katabatic flows (Whiteman 1990). In contrast with the up-slope flows the katabatic flows occur mainly at night and are triggered by the rapid cooling of the slope and the air in its vicinity. Sometimes also referred to as draining flows, katabatic flows are usually less turbulent and are characterized by shallow depths of the boundary layer.

Large amounts of publications have been made over the years on slope flows, but they mainly covered the more stable katabatic flows. The smaller number of available works dealing with anabatic turbulent flows provides evidence for the relative difficulty to investigate up-slope flows. The main reasons are the inhomogeneity and non-stationary nature of the anabatic flow occurring from its strong dependence on thermal forcing and the resulted unstable stratification, which in turn causes buoyancy driven instabilities (Whiteman 2000; Princevac and Fernando 2007; Zardi and Whiteman 2012).

Recent efforts to examine thermally driven flows by means of detecting, observing, and quantifying several important features include the field works (Monti et al. 2002; Demko et al. 2009; Fernando 2010; Choi et al. 2011; Fernando et al. 2015), laboratory experiments (Hunt et al. 2003; Princevac and Fernando 2007; Reuten et al. 2007), and numerical models (Schumann 1990; Noppel and Fiedler 2002; Rampanelli et al. 2004; Fedorovich and Shapiro 2009; Serafin and Zardi 2010). The important features under investigation include thermal forcing, resulted mixing, and turbulence statistics. The examined flows usually characterized by high Reynolds numbers (*Re*), commonly in the range of $\sim 10^3$ to $\sim 10^6$, indicating instability of the flows (Monti et al. 2002; Hunt et al. 2003; Fedorovich and Shapiro 2009). The sought after features of the flows included diffusivity which causes rapid mixing and increased rates of heat/mass/momentum transfer, as well as transport of pollutants (Monti et al. 2002). Also of high interest were the turbulent kinetic energy (TKE) dissipation rates which are difficult to capture due to the need to tap into finer scales of turbulence. The dissipation rates are significant because they are responsible for rapid decay of energy (Tennekes and Lumley 1972; Pope 2000) and play a major role in setting the total energy and mass/heat transfer budget; therefore, they are essential for producing accurate forecasts. Hence, to address the challenges in

weather and climate conditions modelling/forecasting due to the irregularity and stochastic nature of such flows, obtaining comprehensive experimental data on the developing turbulent BL of anabatic flows under various forcing and conditions is highly valuable. Therefore, accurate quantification of turbulent statistical parameters in naturally developing setups in the field is of paramount importance.

As various features of anabatic flows are of paramount importance, such as income velocity, separation length, apex plume, and turbulence structure of the flow, the main focus of this work was the turbulence structure. Turbulent flows are typically considered as flows consisting of various sizes of eddies. The largest are those at which the energy into the flow takes place, energy is then cascaded down into smaller and smaller vortices simply by break-down. The energy cascade stops at very small vortices when kinematic viscosity is dominant. In a fully developed turbulent BL and under the assumptions of local homogeneity and local isotropy of the flow, the Taylors Frozen Approximation (TFA) can be accepted to ease the approximations of the parameters that are used to characterize the flow. Homogeneity of the flow is the first assumption of the TFA, it states that in a fully developed flow, the turbulence statistics of the flow should be the same everywhere in the field. The second assumption of local isotropy defines the flow such that the rate of change of every directional component of the flow should be of the same order and independent of the other components (Kolmogorov 1941).

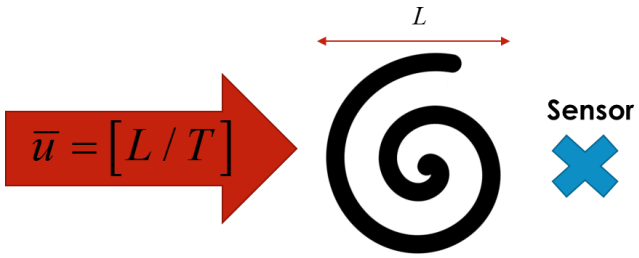

Figure 1.1 Simplified display of Taylor's Frozen Approximation

Figure 1.1 depicts a sketch of an eddy of size L approaching a sensor. T is the time it takes the eddy to pass the sensor, and therefore $\bar{u}$ is the velocity of the eddy. The TFA postulates that we can address eddies of various sizes as being undisturbed, or "frozen," for short periods of time at which they are being translated at the mean velocity of the flow, $\bar{u}$. This approximation is only valid when $u'/\bar{u} << 1$ (Lumley 1965). This simplified

assumption is even more conventional to use in unidirectional flows, and is especially common in BL cases. The unidirectional turbulent velocity flow field is broken down into three components that are traditionally defined in three orthogonal dimensions as *u*, *v*, and *w*. Each component represents a superposition of an average velocity $(\bar{u}, \bar{v}, \bar{w})$ and fluctuations in the corresponding direction (*u'*, *v'*, and *w'*)

$$u = \bar{u} + u', \tag{1.1}$$

$$v = \bar{v} + v', \tag{1.2}$$

$$w = \bar{w} + w'. \tag{1.3}$$

The *u* component of the unidirectional flow field is traditionally the main direction of the flow and has a non-zero average, while the *v* and *w* components are the lateral and vertical components respectively, and have a zero average.

After defining the flow field components, examination of the velocity fluctuations time series enables the derivation of useful calculations of turbulence statistical parameters. It is important to notice that all of the following equations are valid under the assumptions that the flow is unidirectional, locally homogeneous, and locally isotropic. An accepted statistical measure for quantifying turbulence of a unidirectional flow is the turbulence intensity, TI. It is a percentile scale of turbulence defined as

$$TI = \frac{\sqrt{TKE}}{\bar{u}}, \tag{1.4}$$

where the TKE (Turbulent Kinetic Energy) is

$$TKE = \frac{\overline{\left(u'^2 + v'^2 + w'^2\right)}}{2}. \tag{1.5}$$

An explicit *Re* number is commonly used to quantify the upslope/downslope flows using the slope height *D* as the characteristic length scale

$$\mathrm{Re} = \frac{\bar{u}D}{\nu} \tag{1.6}$$

For natural hills and mountains this computes *Re* values in the range of millions which serves no practical use, especially in comparison with laboratory setups. An alternative is the use of an implicit *Re* number, which takes into account turbulent length scales of the flow, e.g.

$$\mathrm{Re}_{\eta} = \frac{\bar{u}\eta}{\nu} \ . \tag{1.7}$$

Here, η is the Kolmogorov microscale (Tennekes and Lumley 1972) obtained from the time series as

$$\eta = \left(\frac{\nu^3}{\bar{\varepsilon}} \right)^{1/4} \ , \tag{1.8}$$

ν is the kinematic viscosity of the flow, and $\bar{\varepsilon}$ is the average TKE dissipation rate. The latter is defined as

$$\bar{\varepsilon} = \frac{\varepsilon_u + \varepsilon_v + \varepsilon_w}{3} \ , \tag{1.9}$$

$$\varepsilon_u = \frac{15\nu}{\bar{u}^2} \overline{\left(\frac{\partial u'}{\partial t} \right)^2} \ , \tag{1.10}$$

$$\varepsilon_v = \frac{7.5\nu}{\bar{u}^2} \overline{\left(\frac{\partial v'}{\partial t} \right)^2} \ , \tag{1.11}$$

$$\varepsilon_w = \frac{7.5\nu}{\bar{u}^2} \overline{\left(\frac{\partial w'}{\partial t} \right)^2} \ . \tag{1.12}$$

Another important parameter defining the nature of velocity fluctuations is the velocity-derivative skewness. This measures the asymmetry of the statistical distribution of the flow's accelerations about the mean acceleration in the main direction of the flow, hence being defined as

$$Sk_u = -skewness\left(\frac{\partial u'}{\partial t} \right) . \tag{1.13}$$

It is an indication of how homogeneous and isotropic the flow is.

Another very important statistical measure of turbulent flows is the power density, *P*, spectrum. The spectrum is broken down into three ranges. The large scale range known as the energy containing range it is the range that consists of input of energy into flow. The intermediate scale range is the inertial subrange where the cascade is not affected by external forces which implies that viscous forces are negligible. Finally, the smallest scale of ranges is the dissipation range, it is the range in which viscosity is no longer negligible. Length scales are commonly used to characterize the flow and denote the different ranges on the spectrum of the energy cascade. The largest length scale is L_H, the horizontal length scale at which the energy input to the cascade occurs, the intermediate is L_T, Taylor's length scale, at which viscous forces can no longer be considered negligible in the energy cascade, and the smallest is η, Kolmogorov length scale, at which viscous forces become dominant and effectively dissipate all the remaining energy into heat.

In 1941 Kolmogorov was able to derive the energy cascade spectral shape by means of dimensional analysis, Figure 1.2, and is described by the following equation

$$P(k) = C\varepsilon^{2/3}k^{-5/3}, \tag{1.14}$$

where, *P* is the power density of each wave number, *C* is known as the Kolmogorov constant and in BL flows is equal to 0.5, and *k* is the wave number. This is a canonical shape known to all of the scientists in the field; it represents the cascade of TKE dissipation in homogeneous and isotopic flows using the famous -5/3 power law.

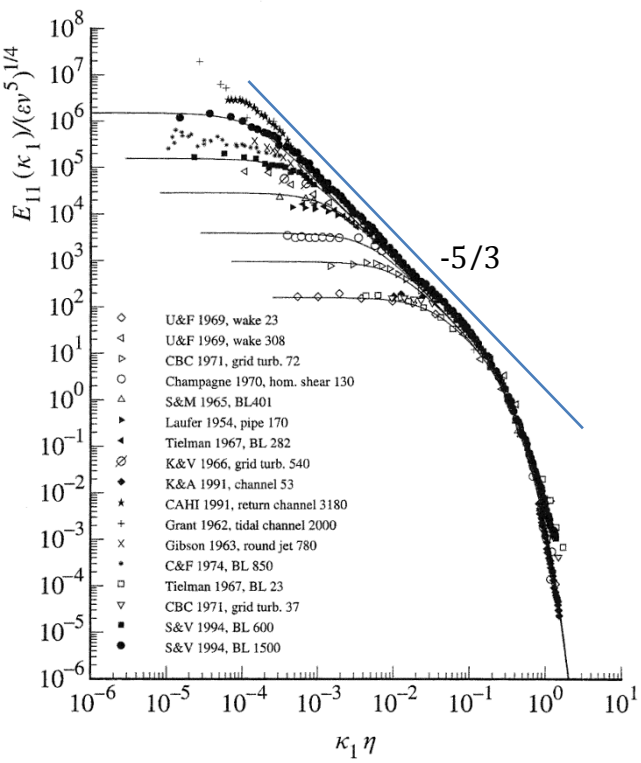

Figure 1.2 Dissipation Spectra Plotted using Kolmogorov's Scaling (Pope 2000)

Unfortunately most natural turbulent flows are anisotropic and not homogeneous and up to this moment no comprehensive and accurate model is available to describe the statistical properties of such flows, and it is therefore common to examine the natural turbulent flows in the field or lab in terms of their deviation from this canonical form.

The need to quantify and examine the detailed above statistical parameters characterizing turbulent flows further emphasizes the importance of the ability to produce accurate measurements of the smallest scales of turbulent velocity fluctuations, preferably in the natural setups of the field. As the aforementioned studies suggest, lab modelling is rather limited and field experiments are certainly hard to perform due to unstable conditions, working at remote locations, etc., especially when taking into account the need to tap into the smallest scales of turbulence under these conditions. The most common device used today to capture a three dimensional flow field is the ultrasonic anemometer (Sonic). The field is a very harsh environment where the temperature, humidity, and average velocity constantly change, and the Sonic is capable of measuring wind speed's fluctuations using the Doppler shift of sound waves being transmitted between orthogonal pairs of transmitters and receivers. The traveling path of the sound waves, λ, sets therefore the spatial resolution of the instrument as it cannot sense the

fluctuations of eddies smaller than λ, the distance between a transducer and receiver of sound waves, that pass the sensor regardless of how high is the sampling frequency.

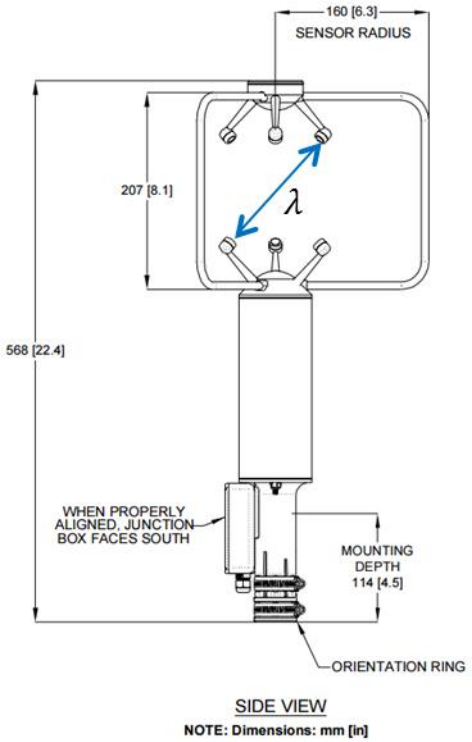

Figure 1.3 Overview of Sonic Manufactured by RM Young, model 81000

Although extremely robust and designed to withstand the harsh field conditions producing continuous measurements of the 3D flow field, the Sonic provides spatially averaged results, and therefore has a limited frequency response. Today, there are various types of Sonics, with sampling frequencies up to 100 Hz. The Sonic used in this study is manufactured by RM Young (model 81000) and has a sampling frequency of 32 Hz; it provides an output of both the three-dimensional field's velocity fluctuations and temperature fluctuations, and has a spatial resolution of 15 cm. In order to derive its frequency response, i.e. the highest trusted frequency, the empirical equation from Kaimal and Finnigan's (see eq. 6.6 1994) is used. In their study, it was shown that Sonic's frequency response is a function of the average velocity and can be defined as

$$f_{max} = \frac{\bar{u}}{L}\ , \qquad (1.15)$$

where $L = 2\pi\lambda$ and is the smallest eddy size the Sonic is capable of detecting. After deriving that $L \sim 0.94\ m$, it can be seen that f_{max} of the Sonic used in this research is of the

same order as the average velocity. In a field with average velocities of $3\,m\,s^{-1}$ this Sonic's data may only be trusted at up to a frequency of ~ 3 Hz.

The current state of acceptable work in the field mainly encompasses the use of slow or low spatial resolution instruments such as Sonics or LIDARS (Light Detection and Ranging) and either extrapolating the obtained spectral shapes to the region of finer scales (usually with a constant dissipation rate) or examining the spectra only at the available large scales range (Hayashi 1994; McNaughton and Laubach 2000; Lothon et al. 2009; Krishnamurthy et al. 2011; Potter et al. 2015). The natural solution should be the use of hot wire/film anemometry as it is capable of producing the fine scale measurements of the velocity fields. These operate by measuring the heat transfer from very thin and short metal wires, which change their resistance as a function of temperature fluctuations occurring from the surrounding flow. In other words, to sense rapid fluctuations, the wires are overheated to a temperature much greater than that of the flow field they aim to sense taking into account the fact that heat transfer rate from the wire to the flow is a function of instantaneous velocity at the wire. Hence, CTA (Constant Temperature Anemometer) works to keep the overheated wire at a constant temperature by continuously adjusting the supplied current, and as the output of the anemometer is usually a voltage relative to this current, this anemometer eventually provides voltage fluctuations relative to velocity fluctuations through a non-linear function that is yet to be determined by calibration.

Due to the configuration of the wires, they are mainly sensitive to the perpendicular component of the flow they encounter, and significantly less sensitive to tangential and transverse components. Increasing the number of wires has the potential to obtain velocity fluctuations derivations by direct measurements, yet provides a calibration limitation, as the major limitation of CTA is in the need to perform a rather complex calibration. Since the transfer function between the output voltages and the sensed velocity of each wire is non-linear, calibration needs to take place in a wind tunnel by exposing the sensors to all of the full range of the expected average velocities as well as to all of the angles of attack to capture the expected fluctuations, a process of several hours. There is also a need for constant recalibration of the wires due to changing conditions in the field (i.e. temperature, humidity, average velocity, and deterioration of the wires exposed to the flow). Therefore, obtaining the full three-dimensional flow field requires use of multi wire probes, and in harsh field conditions, it often means being

stranded by the need of constant re-calibration of the sensors due to changing temperatures and humidity, inevitable contamination, and eventually the degradation of the wire/film sensors, which is a cumbersome task taking into account remote locations and positioning of the probes at various heights.

A recently developed instrument consisting of collocated Sonic and hot-film sensors (HF) is the Combo probe which is based on the proposed work of Oncley et al. (1996) and offers a solution for the main challenges associated with field measurements of turbulent flows. The HF sensors are capable of capturing finer scale turbulence using a constant temperature anemometer (CTA), and collocating the Sonic with the HF allows for simultaneous detection of the same field and provides the Sonic's range of low frequencies as the calibration set that coincides with the voltages provided by the HF. To derive the time series of velocity components' fluctuations from the HF voltages, a continuous *in-situ* calibration against the slowly varying Sonic data was implemented and was based on the NN training method established by (Kit et al. 2010). Details on the Combo design and previous uses can be found in Kit et al. (2010) and Vitkin et al. (2014), including the MATERHORN field campaign only recently reported in Fernando et al. (2015) and Kit et al. (2016); on the most recent study by Kit et al. (2016), the Combo captured the bursting phenomenon. The bursting phenomenon is defined as a period of intense fluctuations of the flow's velocity in short periods of time. It is known as a generation mechanism of the turbulence of flows, and therefore is an important parameter in understanding the physical nature of turbulent flows.

The Combo provides simultaneously sampled data including the low frequency velocities from the Sonic and high frequency voltages from the HF probe. A subset of the data is then selected to comprise a training set (TS) in order to train the NN. Next, the TS undergoes a low pass filter that matches the limited frequency response of the Sonic, and the filtered TS is finally used to train the network, as depicted in Figure 1.4. Once the network is trained, the high frequency HF voltages are fed into the already trained network, and finally high frequency velocity fluctuations are obtained (Figure 1.5). The more detailed description of the NN algorithm is given in Chapter 3. Recent publications listed above have shown the Combo probe's capabilities in field studies including successfully tapping into the fluctuating flows' turbulence with high accuracy and allowing for continuous measurements in harsh field conditions.

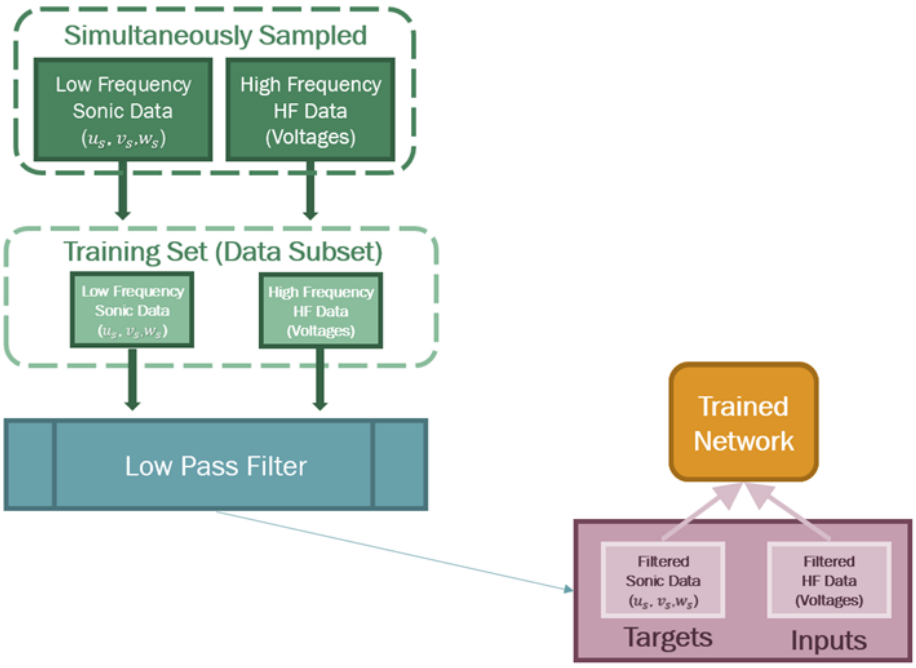

Figure 1.4 Simple flow chart of the *in-situ* calibration process, creating the NN

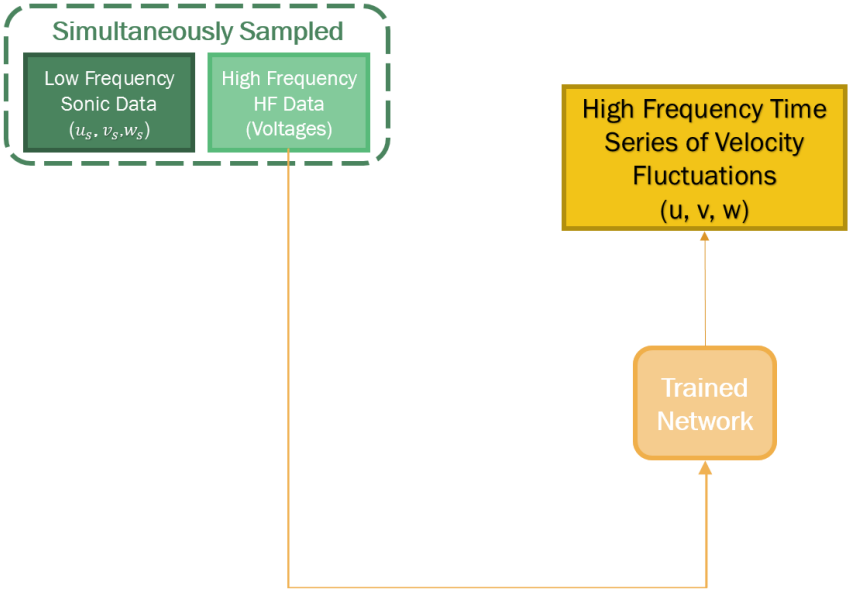

Figure 1.5 Simple flow chart of the *in-situ* calibration process, using the Trained NN

The main goal of this work was to investigate a naturally developing boundary layer of thermally driven anabatic flow by utilizing the newly developed Combo instrument. Setting the instrument in the field will allow tapping into the fine scales of anabatic flow turbulence obtaining continuous measurements of the flow for a period of several days. The collected data will eventually be used to characterize the anabatic flow features by means of statistical analysis, providing fully resolved spectra of all three velocity-field components, deriving empirical fits of important parameters dependence on various non-dimensional numbers, and capturing and examining the bursting phenomenon. The type of flow chosen for this purpose was an unstable up-slope flow that develops by the natural diurnal heating of the slope and often occurs in hilly and mountainous terrains. The appropriate location and methods chosen are elaborated in Chapter 2. Chapter 3 and Chapter 4 provide details on the data processing methods and the obtained results of statistical properties of the measured flow. The results include the fully resolved spectra of the velocity field components and empirical fits to the resolved spectral shapes made available for future research performed with slow instruments.

Chapter 2 Experimental Setup

A field experiment was staged to identify and quantify important parameters characterizing the thermally driven anabatic flow in absence of background forcing. A moderate slope located on the south-western side of Nofit (Figure 2.1), a communal village in the northern part of Israel (latitude 32.7551° and longitude 35.1415°), was chosen as the location of measurements due to its favorable topography and easily accessible power and communications. Situated on the low hills some 15 kilometers inland, the site is naturally shielded from possible offshore breeze. The time of year chosen for the measurements was in the peak of the 2015 summer, between August 8th and August 16th, to minimize anabatic flow perturbations by vegetation and to minimize the chances to encounter significant synoptic forcing. Indeed, during the 8 days of measurements, zero cloud coverage and no synoptic systems were recorded.

Figure 2.1 Nofit's Relative Location on the map (taken from Google maps, 2016) and an aerial view of the slope (from govmap.gov.il, 2014). The exact location of measurements is marked in the red circle (latitude 32.7551° and longitude 35.1415°).

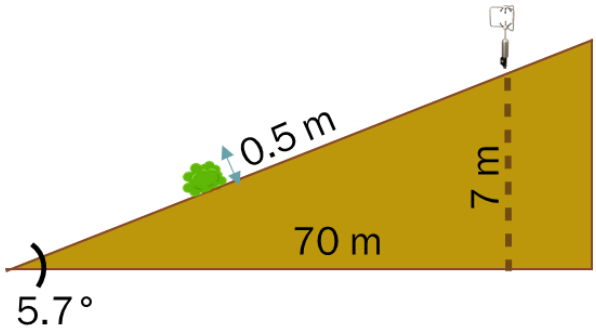

Figure 2.2 Side view of the Slope

The measurements were taken on the edge of the rocky slope with minimal natural vegetation facing the south-western side of the hill constituting a 5.7° slope as depicted in Figure 2.2. The distance from the location of measurement to the street above was approximately 30 meters and was obstructed by a line of houses, so no development of significant down-slope flows were recorded during night hours. The elevation variation between the points where measurements took place to the bottom of the slope is 7 meters, and the distance between the two points measured 70 meters.

The site was instrumented with various probes and data acquisition equipment to allow continuous measurements of the three-dimensional-wind-velocity field and the local distribution/concentration of common pollutants. In this work only wind field results are reported.

A Combo probe (Figure 2.3), similar to the one used in Hocut et al. (2015) and Fernando et al. (2015), was deployed at the top of a two meters high mast providing high frequency measurements of all three velocity components' fluctuations. The Combo was composed of RM Young's Ultrasonic Anemometer model 81000 (hereinafter Sonic) and two orthogonal X-shaped hot film probes manufactured by TSI (model 1241-20W, hereinafter HF) mounted on an automatically motorized rotating holding arm. According to the method described below, the low time and spatial resolution signal of the Sonic was used to perform the *in-situ* calibration of HF voltages. Constant re-alignment of the HF probes with the mean wind direction was achieved by rotating the holding arm using a coupled stepper motor (NEMA-17) and a digital encoder (US Digital's HD52A) that provided radial accuracy of one tenth of a degree.

Figure 2.3 Two measuring instruments
on the left side of the image are the AQMesh (pyramid shaped device)
and inside the plastic cage is the laser particle counter;
on the right side of image is the Combo including:
Ultrasonic Anemometer and two X-shaped hot film probes.

The Sonic was programmed to sample at its maximum frequency of 32 Hz and provided an analogue output of the three velocity components' (u, v, and w) and the temperature's (T) time series. The HF sensors used in this field experiment (1.02 mm long and 0.05 mm wide each) are designed for liquid application and were selected for their higher robustness relative to the traditional thinner films/wires. One X-shaped HF sensor was oriented horizontally and the other vertically, hence providing voltage fluctuations across the films about u, v and u, w velocity components accordingly. The redundant information of the u velocity component was used to improve the signal-to-noise ratio by means of averaging. Since the u component is the one of the main flow, positioning both 2D sensors in a way to allow obtaining all three velocity components simultaneously, while keeping the probe stem aligned with the mean flow to assure acceptable angles of attack, results in the u component specifically being sensed independently by both sensors. Hence it was possible to increase the signal-to-noise ratio of u component by averaging both signals, effectively reducing the ratio of random noise to the coherent velocity fluctuation signal. The HF sensors were driven by four MiniCTA channels (Dantec

Dynamics model 54T42) with an overheat ratio set to 1.5 and an installed 1 kHz low pass filter in the miniCTA hardware. The selected high overheat ratio increases the velocity sensitivity to the temperature sensitivity ratio, which improves the dynamic response in a non-isothermal flow (Bruun 1995). Rotation of the HF sensors, placed several millimeters from the center of the Sonic's control volume, was performed in a way that the sensors themselves remained in place while only changing the direction to follow that of the mean wind. Sonic's data were used to determine the required alignment direction of the sensors; once every 60 seconds, an average wind direction of the last 5 seconds was obtained to determine the next rotation angle and the new positioning of the sensors for the upcoming 60 seconds of measurements. After the rotation was performed, the actual new direction was recorded from the readings of the encoder. The rotation angle, and hence the measurable angle of attack of the mean wind speed, was limited to a 120 degrees span due to the geometrical restriction imposed by the Sonic's support struts.

In addition to the Combo sensing the turbulent upslope flow velocities, two arrangements of air quality monitoring systems were installed at the site of measurements (see left side of Figure 2.3). These included the AQMesh air quality monitoring system and the Dylos laser particle counter (model DC1700). The AQMesh monitored NO_2, O_3, CO, temperature, and humidity. The two air monitoring systems arrangements were set up at 2 and 0.2 meters above ground respectively. Both AQMesh instruments recorded average temperatures over 15 minute intervals. Here, only the temperature records provided by the AQMesh are considered.

The data collection and the control of the Combo were performed by a specially written LabView routine running on the mini field PC equipped with a National Instruments USB-6211 data-acquisition board. Continuous recording of all Combo data (four Sonic, four HF, and one encoder channels) was performed simultaneously at 2 kHz sampling frequency in 60-second-long intervals. To derive the time series of velocity components' fluctuations from the HF voltages, a continuous *in-situ* calibration against the slowly varying Sonic data was implemented—based on the NN training method established by (Kit et al. 2010). After setting up the instruments in the field, data acquisition was performed continuously for 8 days, resulting in series of both Sonic provided three velocity components (at 32 Hz) and four HF voltages (at 2 kHz), all recorded simultaneously at 2 kHz, hence obtaining series of 120,000 data points long

records (60 seconds) for each constituent. All sonic velocity records $(u_s\ v_s\ w_s)$ were then translated into the HF probe's coordinate system components $\left(u_p\ v_p\ w_p\right)$ by

$$u_p = u_s \sin(\alpha) + v_s \cos(\alpha), \tag{2.1}$$

$$v_p = -u_s \cos(\alpha) + v_s \sin(\alpha)\ . \tag{2.2}$$

α denoted the corresponding minute-long record's alignment angle and w_p was kept unchanged from the original records as the HF sensors performed only yaw rotation. Next, all data were examined to determine which minute-long records are suitable for further processing by the NN based calibration method. Averages of each velocity component $\left(\overline{u}_p\ \overline{v}_p\ \overline{w}_p\right)$ were calculated and appropriate minutes, during which the flow velocity was judged to be sufficiently unidirectional $\left(\overline{u}_p \geq 6\,\overline{v}_p\right)$ and aligned with the HF sensors for the duration of the entire minute, were selected for further processing. The average vertical velocity component $\overline{w}_p$ was found always to be significantly smaller. The selected records were split into groups not exceeding one hour of total time span during which both the temperature and the humidity in the flow field remained adequately constant.

Chapter 3 Data Processing

As mentioned in the previous chapter, prior to the data processing method described in this chapter, a selection of eligible minutes is necessary based on the criteria described below. The initial condition was for the average velocity to be $\overline{u}_p \geq 2\, m\, s^{-1}$ to exclusively examine the fully developed flow. The direction of the flow needed to correspond to the 120° span imposed by the Sonic's support struts, and to be aligned with, $\alpha \pm 10°$, the actual orientation of the HF probe derived from the reading of the encoder. Finally, the flow was required to be judged as sufficiently unidirectional, where $\overline{u}_p \geq 6\overline{v}_p$. After discarding the non-eligible minutes, a total of 429 eligible minutes remains and is presented in Figure 3.1. Next, the minutes were rearranged into 1 hour intervals in order to train unique networks for each hour in which the calibration is reliable due to the relatively similar conditions of temperature, humidity, and deterioration of the HF.

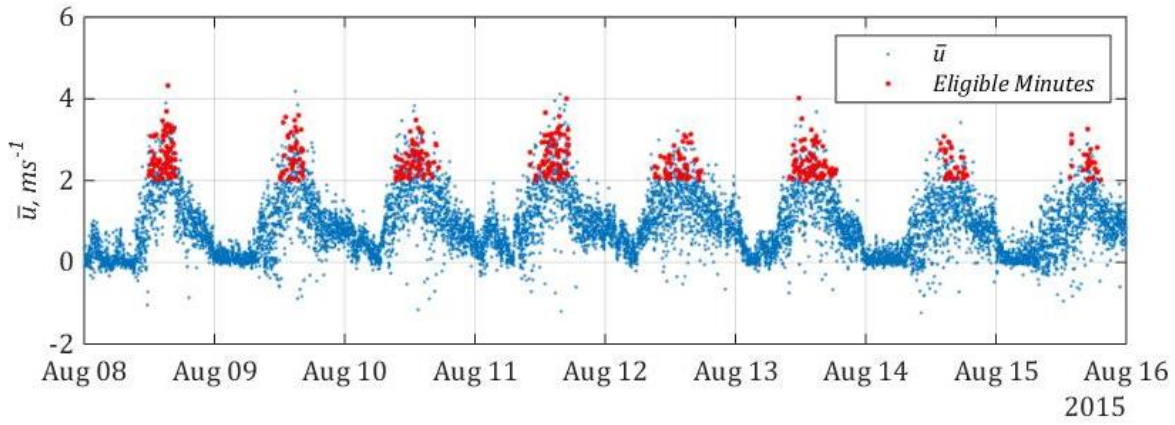

Figure 3.1 All 429 eligible minutes for *in-situ* calibration

Each group of records consisted of the Sonic's velocities and of the HF's voltages. The heated HF's exposure to a flow causes a change in resistance/voltage corresponding to the change of the flow's velocity field, and a transfer function was necessary to convert the voltage outputs to velocities. The HF outputs were *in-situ* calibrated using NN based velocity-voltage transfer functions (Kit et al. 2010) where, again, each transfer function was reliable for the period of one hour. The variation in spatial and temporal resolutions provided by Sonic and HF probe was bridged using a low pass filter, equivalent to the

maximum reliable frequency of the Sonic (i.e. the limit of its frequency response), as the same field was sensed by both instruments at low frequencies.

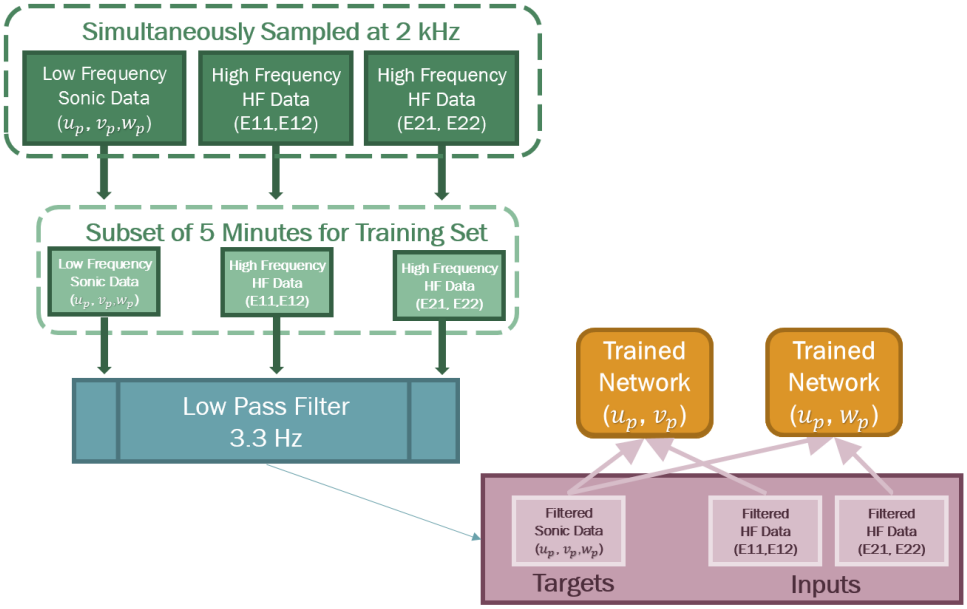

Figure 3.2 Preparation for NN Training

Figure 3.2 depicts the detailed calibration process for each group of data points within a 1-hour interval. Each NN was trained using its own training set (TS) containing low pass filtered velocities and voltages carefully selected from the same hour ensemble of eligible minutes. Each TS consisted of 5 minutes whose root mean square of the u_p component was closest to unity and the $\bar{u}_p$ best represented the entire range of average velocities for that hour, providing a total of 600,000 data points. The filtering was performed by block averaging the data into 600 data point blocks, equivalent to the aforementioned trusted Sonic's output range at a lower cut off frequency of 3.3 Hz, which created a TS of 1,000 data points. Each data point consisted of 4 HF voltages and their respective 3 velocity components from the Sonic. Each network was then trained using the HF voltages as inputs and the Sonic's velocities as targeted outputs. To increase the signal-to-noise ratio of the high frequency velocity fluctuation signals, two separate NNs were trained each time: one for the *u* and *v* components from the horizontally oriented HF probe, and one the *u* and *w* components from the vertically oriented HF sensor. Once trained the networks were fed with the high frequency HF voltages series from a corresponding probe (Figure 3.3). Next, an average of two resulted u_p components of velocity fluctuations was taken, finally, high frequency time series of all three field velocity

fluctuations were obtained. After the two NN were trained for every hour, velocities were derived for all sufficiently unidirectional minutes previously selected within that hour. The obtained time series were examined and turbulence statistics (TI, TKE, skewness, dissipation rates, Kolmogorov length-scale) and spectra were produced.

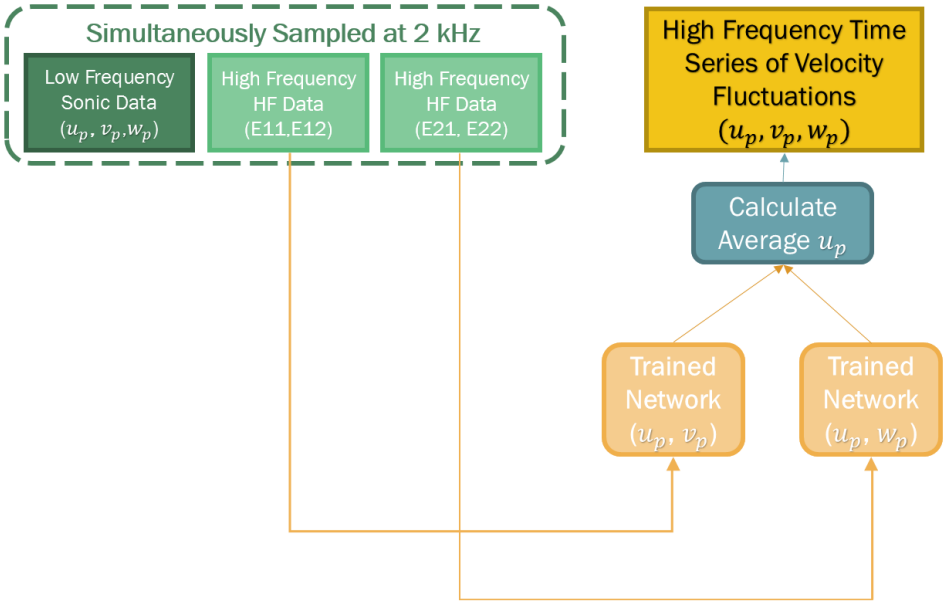

Figure 3.3 After obtaining trained network, feed high frequency data

The confidence in accuracy of the NN based *in-situ* calibration for conditions experienced in these measurements mainly relies on the previous results reported in (Kit et al. 2010; Kit and Liberzon 2016), where NN method was tested against accurate standard calibration sets both in wind tunnel and in free jet. However a necessary confidence test, a TS self-reconstruction, was performed to assure correctness of all chosen parameters used in NN training process. In Figures 3.4-3.5, the normalized self-reconstruction test of a representative data set from both HF sensors are presented. In this test the trained NN reconstructs the TS itself that was used to train it. Figure 3.4 displays the data obtained from the horizontal HF sensor (*u v*), while Figure 3.5 displays the vertical sensor's (*u w*). The normalization was calculated by subtracting the average component of each series and then dividing by the rms of the series to get a percentile perspective. The dot ensembles represent the original targets that were used to train the network, while the lines represent the self-reconstructed targets. The normalized outputs follow the trend of the expected outputs and provide a confirmation that the reconstructed TS were reliable, as the reconstructed results compare well, presenting

high accuracy of fluctuations reconstruction, and confirming the turbulence is well captured. Furthermore, both reconstructed *u* ensembles from both sensors are very similar, and an increase in the signal to noise ratio is obtained by taking an average of the two.

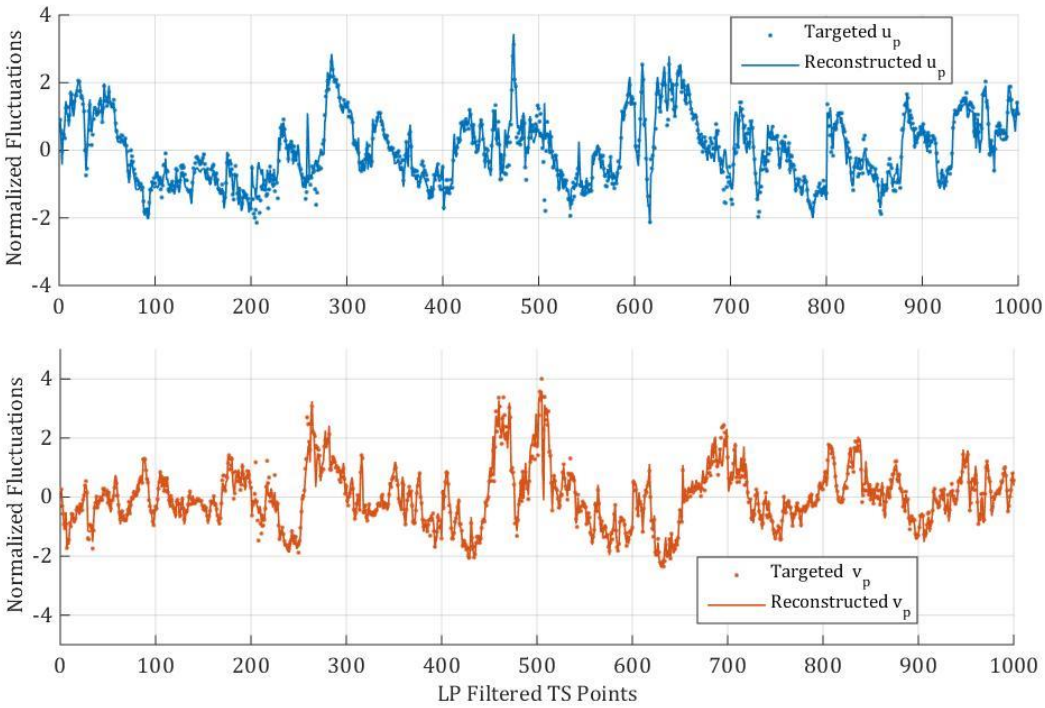

Figure 3.4 Normalized self-reconstruction of horizontal HF sensor's training set

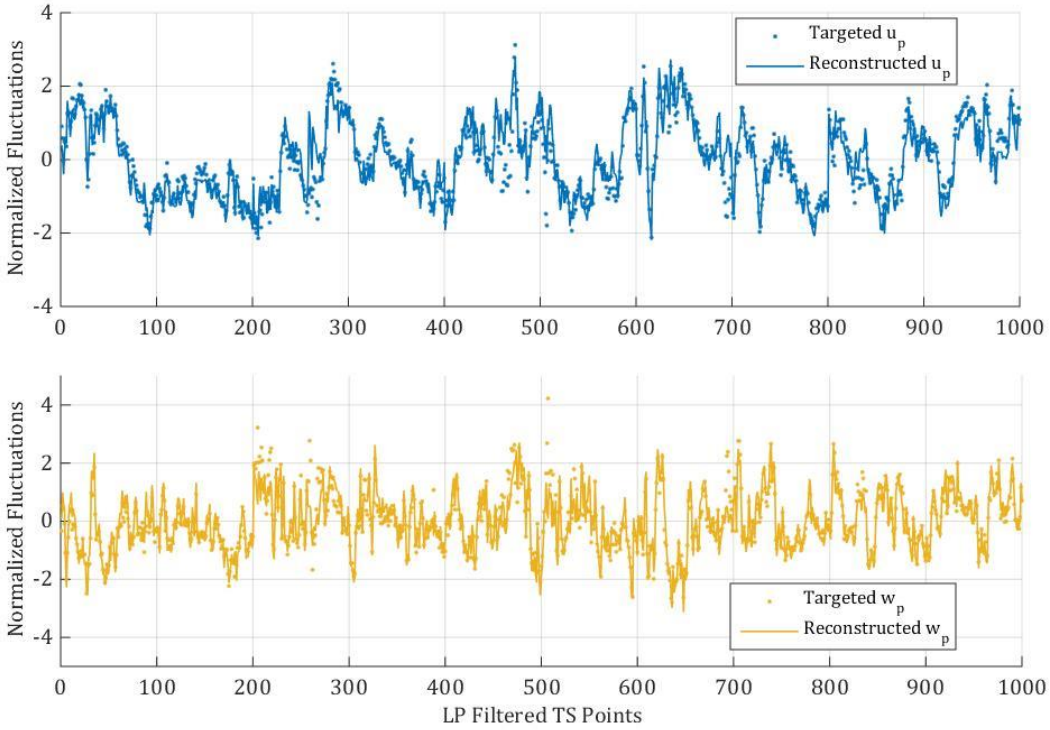

Figure 3.5 Normalized Self-reconstruction of vertical HF sensor's training set

An example of a reconstructed time series is displayed in Figures 3.6-3.8. The *u* component is displayed in blue, and the *v w* components are in orange and yellow respectively. As expected the *u* component is of a non-zero average, and the *v* and *w* components fluctuate around a value close to zero, rendering this flow field unidirectional. Figures 3.6 and 3.7 zoom in to intervals 5 seconds long and 1 second long respectively to observe the high frequency fluctuations obtained, presenting typical turbulent fluctuations of the flow.

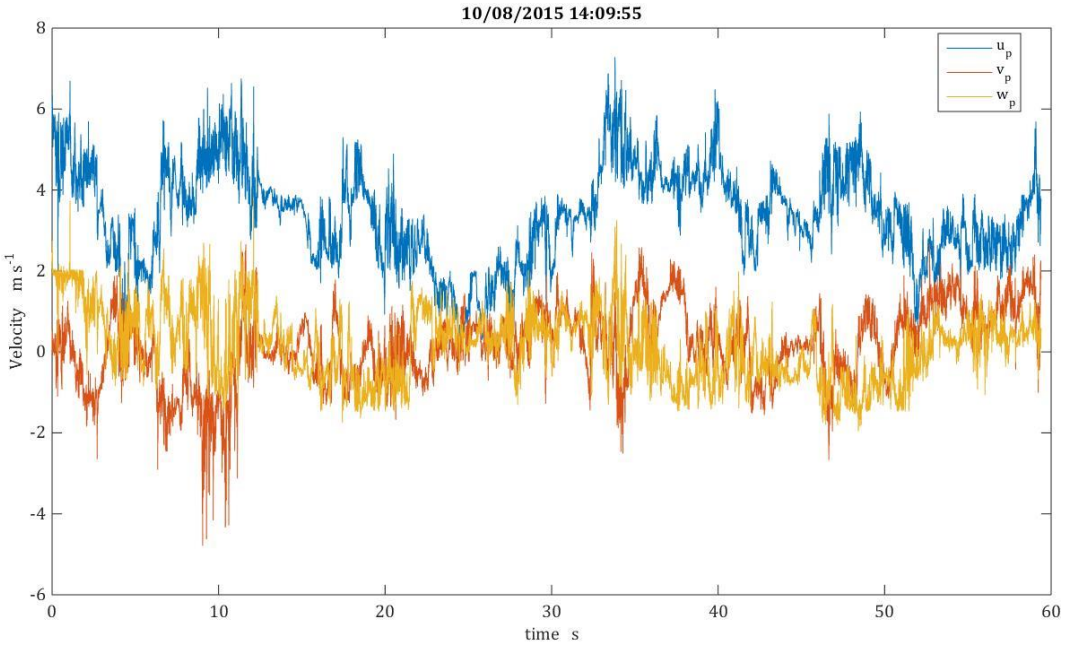

Figure 3.6 Representative reconstructed time series of all three velocity field components, 60 s

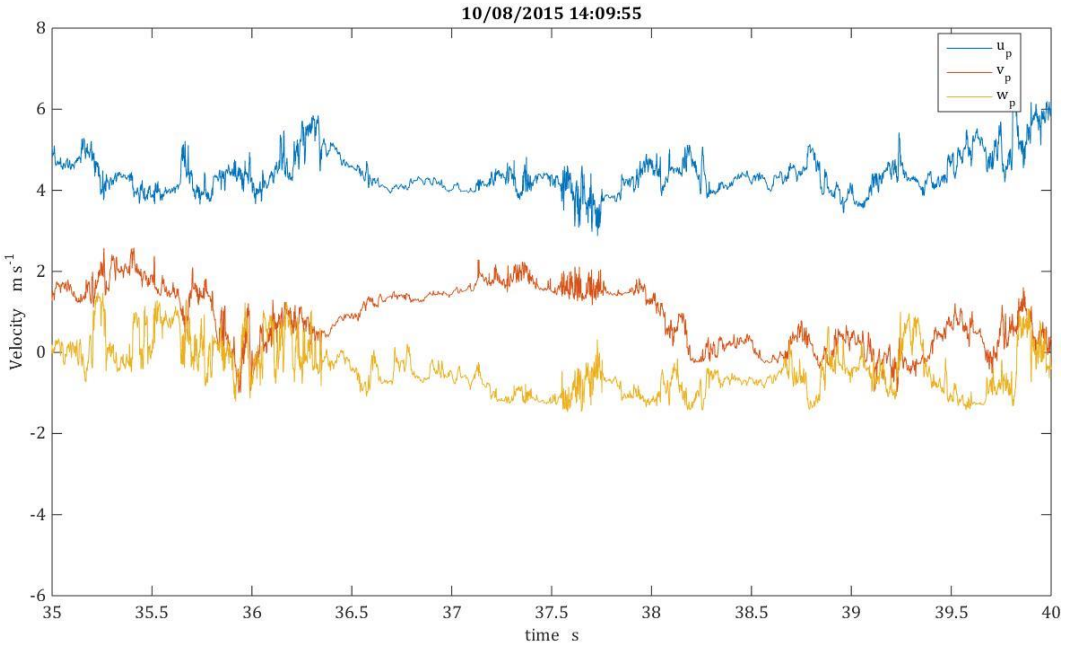

Figure 3.7 Representative reconstructed time series of all three velocity field components, 5 s

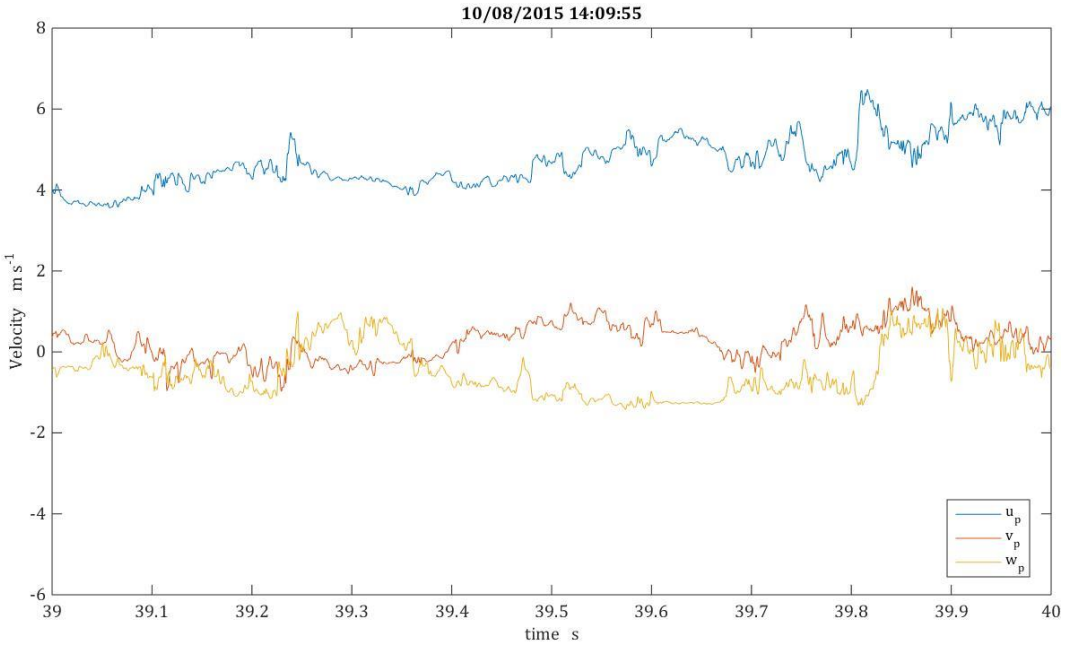

Figure 3.8 Representative reconstructed time series of all three velocity field components, 1 s

Chapter 4 Results

4.1 Mean Flow

After obtaining the results from the field, the initial step was to confirm that the examined flow is indeed anabatic and driven by thermal forcing. Figure 4.1 displays distribution along all 8 days of measurements of average velocities, wind direction in terms of meteorological angle, temperature fluctuations, and vertical temperature gradients. These data indicated the presence of the diurnal pattern as velocity fluctuations are following those of temperature. The wind direction was found to be aligned with the slope when the flow is significant, expressing that thermally driven up-slope diurnal cycle was successfully captured. At the peak, average velocity was reaching $3-4\,m\,s^{-1}$ flowing up the slope at ~ 270 ° meteorological angle. The wind speed peaks occurred at the maxima of temperature gradients; all together indicating the development of a thermally driven anabatic flow. The temperature gradients were ~1° Celsius and were lagging behind maximum recorded temperatures. It is important to note that during night hours no significant flow was observed as no katabatic flow can develop due to the blocking from the line of houses. After observing the diurnal pattern, next the data was normalized to characterize daily changes of important parameters.

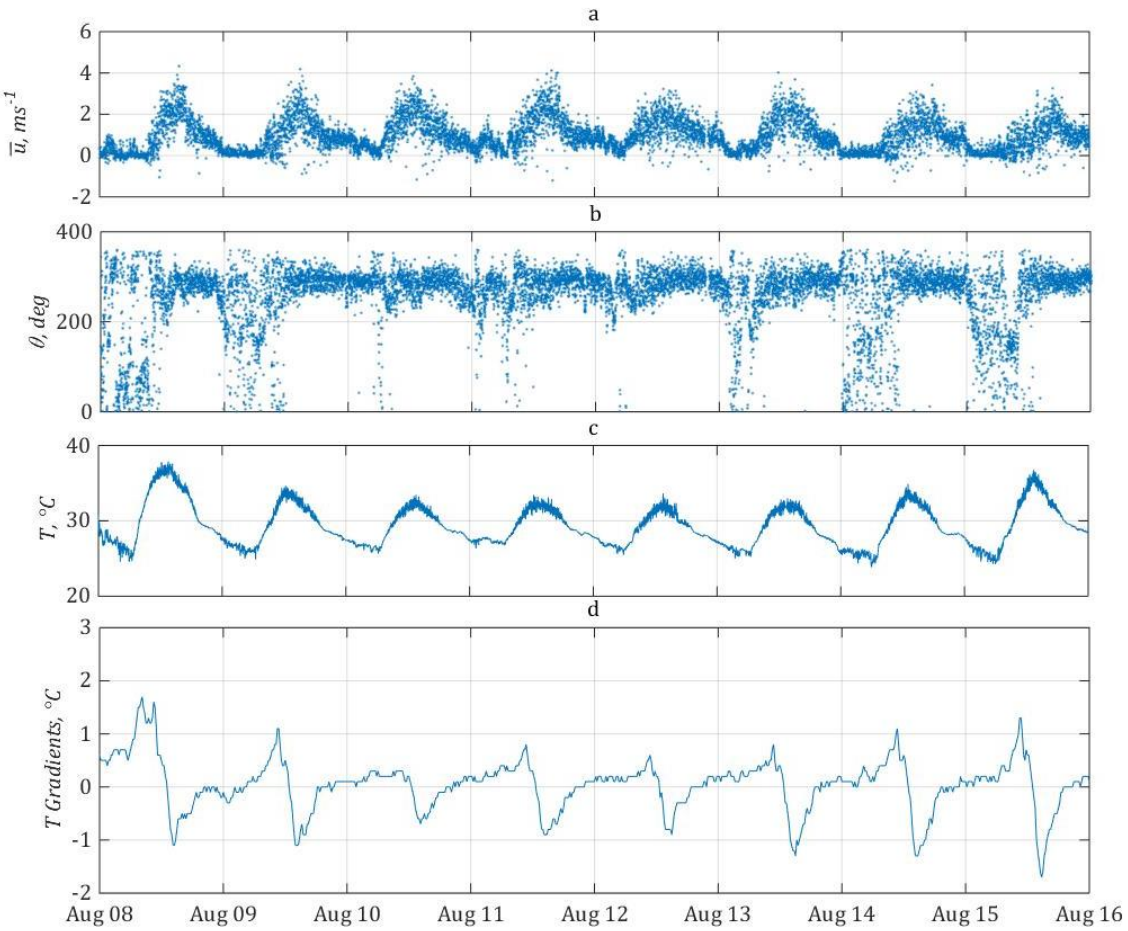

Figure 4.1 Data recorded on all 8 days

(a): average wind velocities $(\bar{u})$ of every recorded minute

(b): meteorological direction (θ) of the wind

(c): temperature (T) at 2m above the ground obtained from the Sonic and

(d): temperature gradient fluctuations along the 8 days of measurements $(\Delta T = T_{2m} - T_{0.2m})$.

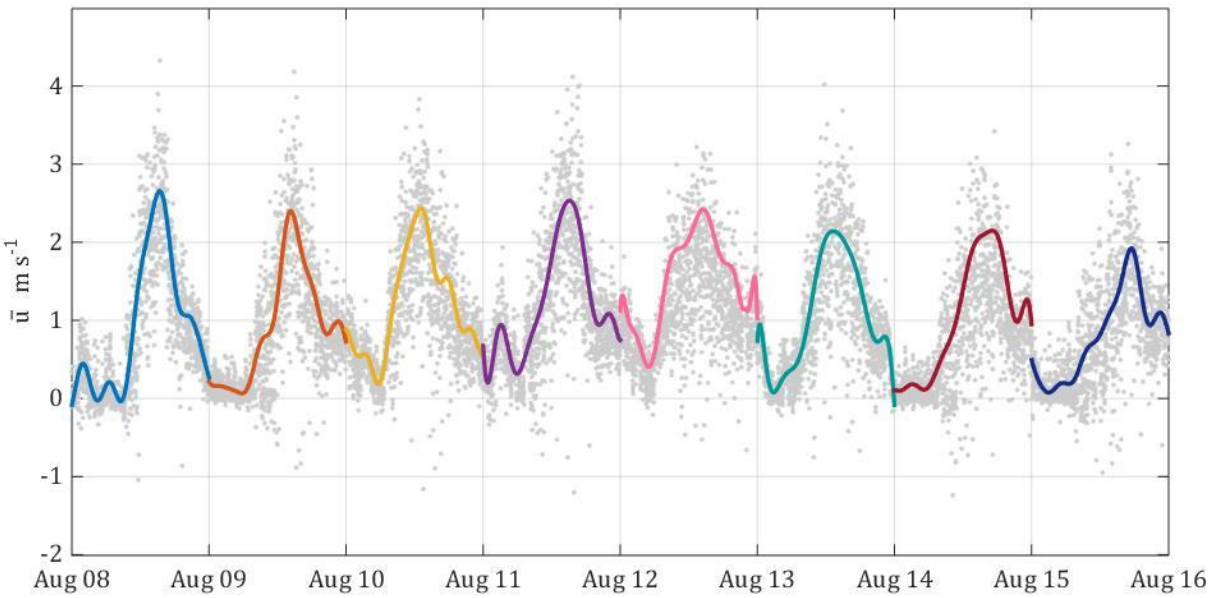

Figure 4.2 Curve fitting of daily average velocities

First, the average velocities of the flow were examined for each of the 8 days. The large average velocity scatter is typical for unstable turbulent flows, and therefore curve fitting was necessary to represent each day. Figure 4.2 displays the curve fitting, using a 6-harmonics Fourier series, of the diurnal observations of mean velocity that was used to obtain maximum representative average velocity per day. Discontinuity in mean velocity values distribution seen between August 12-13, August 14-15, and August 15-16 is the result of short system shut down times at night hours performed for the sake of maintenance. Each of these curves provided a maximum that was used to normalize the average velocity ensemble of each day. Figure 4.3 displays the normalized average velocity fluctuations that were normalized to the respective daily maximum velocities during a 24 hour period. The red curve in Figure 4.3 is a representative curve of the mean velocities and was calculated using a 2nd-order-Gaussian fit by a least-squares method. It presents the diurnal cycle of the mean wind velocity change over 24 hours. The data ensemble represents one-minute-mean-wind-speed values collected during all 8 days of measurements and plotted against the respective time of measurement. The ensemble distribution forms a distinctive pattern as follows: an increase from virtually zero motion shortly after sunset, followed by a rapid increase in wind speed until the maximum is reached during early afternoon, and a graduate decrease of the mean-wind speed toward the sunset time and beyond. No significant flow was measured during the night. Such a pattern indicates the presence of a thermally forced unstable stratification of the air mass

on the slope. As the sun heated the slope's surface, some of the heat was convected to the air at lower levels. This increased the buoyancy of the latter which in turn rose and eventually formed a turbulent BL of an anabatic flow (Stull 1988, Whiteman 1990). The upslope flow in the BL is highly turbulent, as seen from turbulence statistics analyzed later in the text.

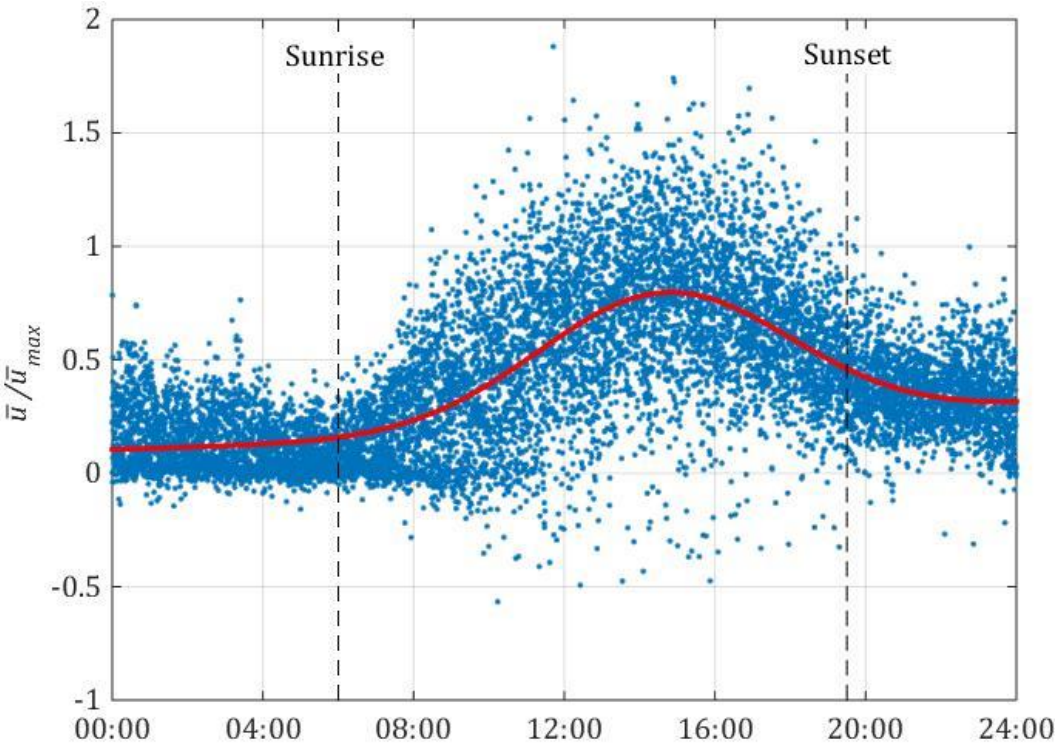

Figure 4.3 Normalized average velocities $\left(\overline{u}/\overline{u}_{\max}\right)$
representing the diurnal cycle during the 8 days of measurements.
The red curve represents a fit of the normalized average velocities of all 8 days.

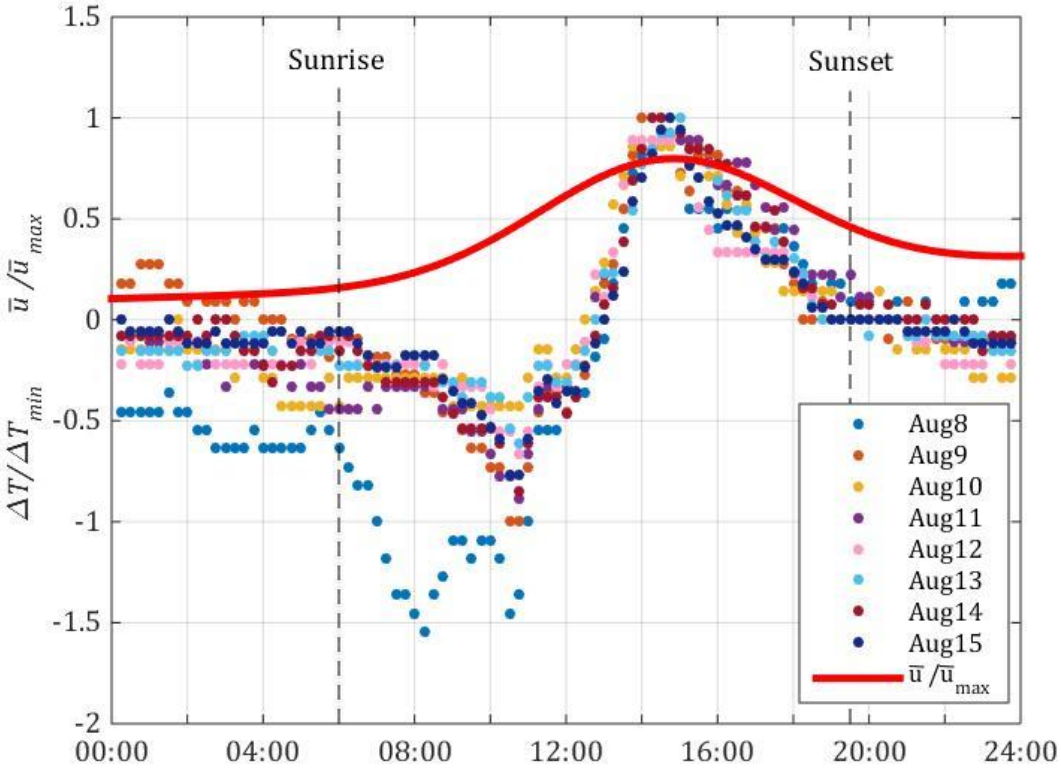

Figure 4.4 Normalized Daily Temperature Gradients

ΔT fluctuations normalized to the respective daily maximum.

Sunrise of each of the 8 days occurred at 6 am and sunset at 7:30 pm.

After observing the normalized diurnal cycle of the average velocities, the diurnal cycle of normalized temperature gradients is examined, as depicted in Figure 4.4. Here, the temperature gradients, recorded at each of the 8 days of measurements and normalized to the respective daily minimum, as it indicates peak of unstable stratification portion of the day, were plotted together with respect to the time of day. This plot demonstrates very well the thermal forcing of the flow. At night, the temperature gradients are virtually zero, as the sun rises, it heats the ground and air together. The air is heated quicker than the ground and a positive gradient is developed. It is depicted as a negative change in Figure 4.4 because these temperature gradients were normalized to the respective daily minimum. As radiation heating continues and increases toward noon the rocks become hotter than the surrounding air mass, eventually changing the temperature gradient sign. As soon as temperature gradients become negative, the flow becomes unstably stratified. The hotter air below wants to rise while the cooler air wants to sink and significant upslope flow is being generated. Average velocity reaches maximum when temperature gradients are at a minimum sometime after noon. As the

sun begins to set down, the temperature gradient's negative values begin to decrease, reducing thermal forcing and hence a drop in the upslope velocity is observed. Several hours after sunset, temperature gradient and average velocity are zero again, and the same process is repeated daily. All days' data ensembles indeed showed a similar behavior reaching maxima shortly after noon, with the exception of August 8th, which is explained by higher mean temperature recorded that day (see Figure 4.1). This is consistent with the mean-wind-velocity records' behavior discussed above. Temperature gradients and velocity fluctuations showed a strong correlation, again indicating thermal forcing of the examined anabatic flow.

4.2 Turbulence Statistics

After confirming the thermally driven nature of the observed anabatic BL flow given the aforementioned results and diurnal inclinations, the turbulence statistics were examined. This was performed by obtaining statistical parameters (TI, TKE, velocity derivative skewness, average TKE dissipation rates, *Re* numbers) and spectra from the time series of velocity fluctuations. The kinematic viscosity of air at the recorded temperatures was taken to be $\nu = 1.6\times10^{-5}$ m^2 s^{-1}, and remaining constant for all processed data. Implicit *Re* values, calculated using the slope height of 7 meters as the characteristic length scale, were in $\sim10^6$ and therefore impractical. Instead, the Kolmogorov length scale η was used as the characteristic length scale providing explicit Re_η from (1.7). Turbulence statistical parameters in literature are commonly presented with respect to *Re,* the use of an implicit Re_η using η as the characteristic length is a very common practice that allows comparing turbulent flows in a wide range of setups in terms of non-dimensional Reynolds number. Using the *in-situ* calibration of the HF sensors allowed for the velocity fluctuations to be obtained at a high sampling rate of 2 kHz, and the power density, *P*, spectra of all three velocity components were calculated for all available one-minute-data sets. Spectra were obtained by performing windowed Fourier Transform calculation in 2.048-second long windows, effectively producing average power spectra of each 120,000 long one-minute with 0.488 Hz frequency resolution. Figure 4.5 below presents the spectra of four representative measured minutes from August 9th and August 10th. As mentioned above, all hereinafter velocity components are in the coordinate system corresponding to the actual HF orientation, i.e. u_p is the velocity along the HF holder and v_p and w_p are the longitudinal and the vertical components correspondingly. Spectra of all velocity components exhibited shapes typical for turbulent flows, presenting an energy cascade down the smallest scales. The energy cascade however was not constant but changed, providing initial indication that the examined turbulent flow was not homogeneous.

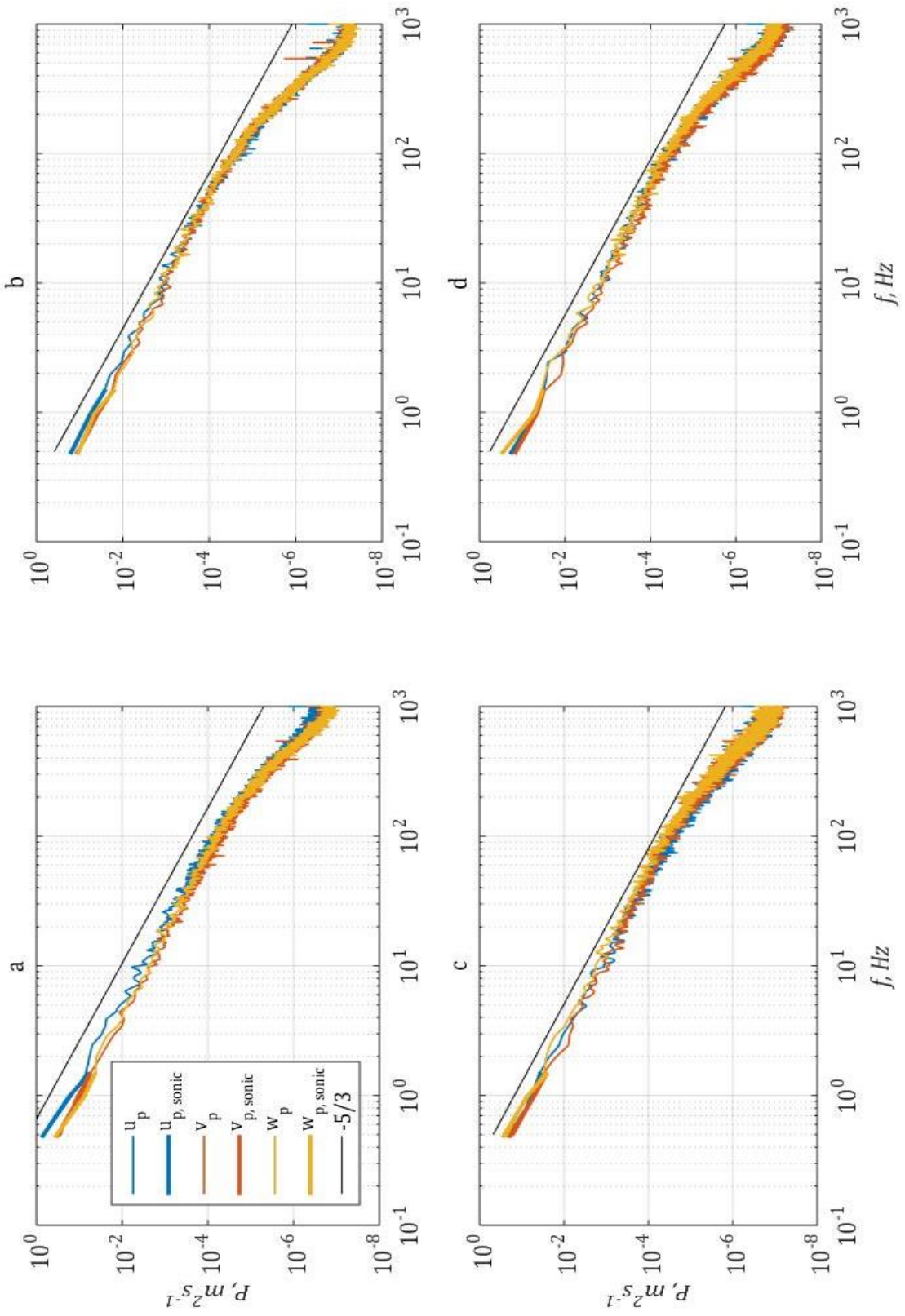

Figure 4.5 Four independent minutes' fully resolved spectra and their respective turbulence statistics.
(a) August 9th at 3:08 pm. *TI* = 32.5% , *TKE* = 1.586 $m^2 s^{-2}$, *Sk* = -0.329, $\overline{\varepsilon}$ = 0.104 $m^2 s^{-3}$, Re_η = 107.9.
(b) August 9th 4:17 pm. *TI* = 29.3% , *TKE* = 0.493 $m^2 s^{-2}$, *Sk* = -0.565, $\overline{\varepsilon}$ = 0.082 $m^2 s^{-3}$, Re_η = 70.8.
(c) August 10th at 11:17 am. *TI* = 30.6% , *TKE* = 0.814 $m^2 s^{-2}$, *Sk* = -0.243, $\overline{\varepsilon}$ = 0.087 $m^2 s^{-3}$, Re_η = 85.9.
(d) August 10th at 3:10 pm. *TI* = 31.6%, *TKE* = 0.796 $m^2 s^{-2}$, *Sk* = -0.516, $\overline{\varepsilon}$ = 0.109 $m^2 s^{-3}$, Re_η = 77.7.

In a few, approximately 15%, of the examined minutes' spectra, the transition to a higher dissipation rate was found not to be smooth, but characterized by a large "bulge" (Figure 4.6b, d), indicating the presence of a so called "bottleneck" effect (Falkovich 1994, Saddoughi and Veeravalli 1994, Tatarskii 2005). A visual examination of the corresponding time series (Figure 4.6a, c) of velocity fluctuations revealed presence of a bursting phenomenon similar to the findings of Kim et al. (1971) and Narahari et al. (1971) in liquid. The bursting phenomenon is common in thermally driven flows. A previous work, currently under review with the *Journal of Fluid Mechanics*, conducted in Dugway Proving Grounds, Utah USA, used the Combo as its measuring instrument and noticed both the presence of the bottleneck bump on the spectra and the visual representation of bursting in the corresponding time series (Kit et al. 2016, see Appendix). In their work, stable BL flows were captured and bottlenecks were observed at frequencies ~100 Hz; in this work, unstable BL flows were examined and bottlenecks were observed at lower frequencies ~60 Hz. The variation in stability of BL between the two mentioned records can be the reason for deviation in frequencies at which the bottleneck occurred. Bursting is of great importance because it is commonly believed to be one of the primary energy generation mechanisms in the BL (Kim et al. 1971, Davidson 2004). The ability to capture bursting in a natural BL of relatively low mean speed is highly advantageous and is conceivable due to the use of the Combo, further discussion of the bursting phenomenon is available in Section 4.3.

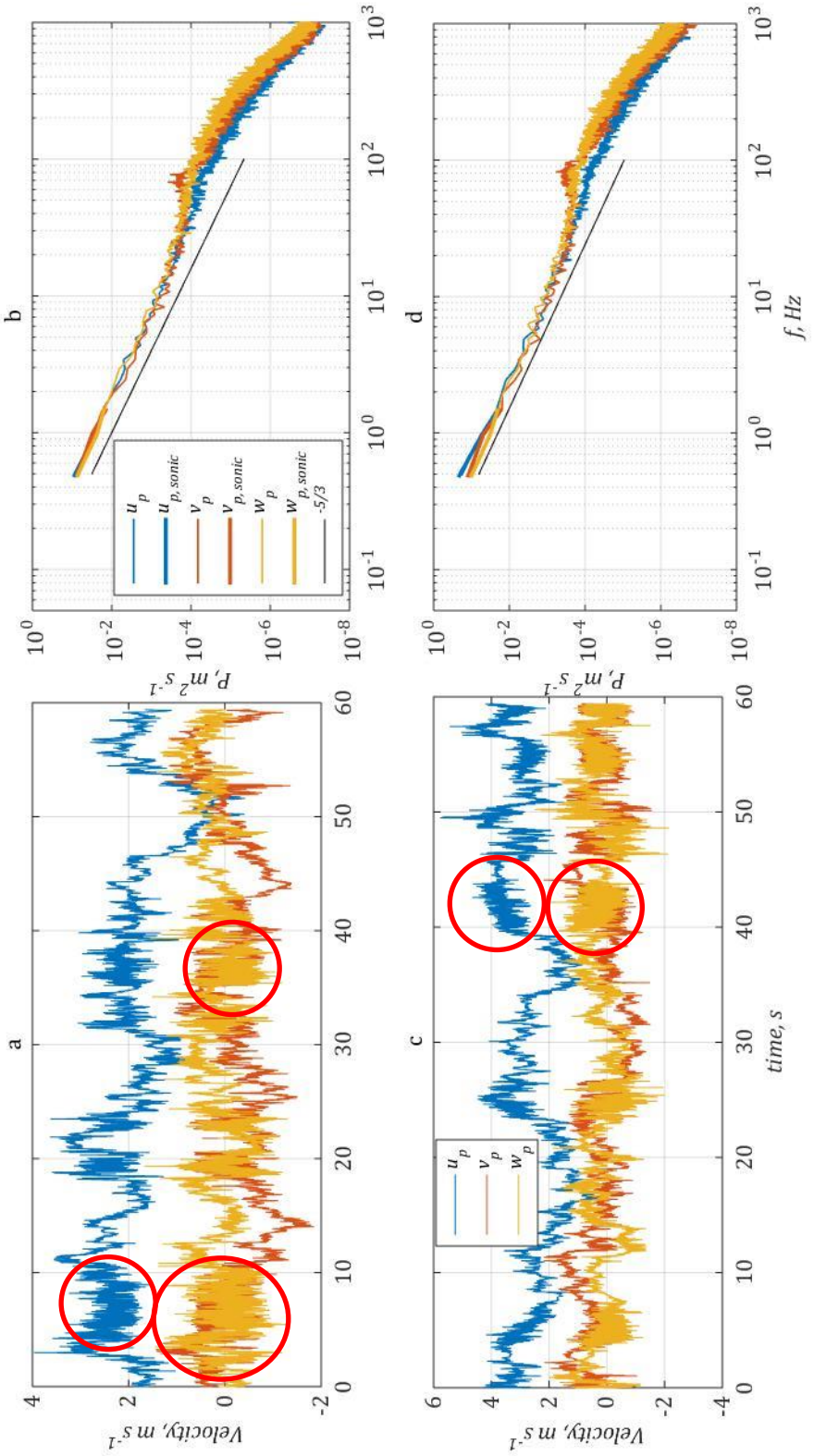

Figure 4.6 Observation of Bursting phenomenon

Time series and spectra of two independent minutes demonstrating the observed occurrence of bursting. The red circles in (b) indicate the visual representation of bursts in the time series.
(a): Reconstructed time series and (b): respective spectra of August 10 at 9:27 am:
TI = 35.9% , TKE = 0.475 m^2 s^{-2}, Sk = -0.322, $\overline{\varepsilon}$ = 0.385 m^2 s^{-3}, Re_η = 38.6.
(c): Reconstructed time series and (d): respective spectra of August 12 at 10:57 am:
TI = 33.4% , TKE = 0.784 m^2 s^{-2}, Sk = -0.269, $\overline{\varepsilon}$ = 0.485 m^2 s^{-3}, Re_η = 50.6.

In Figure 4.7 the average velocity is represented by an increasing trend when presented against Re_η. Minutes in which bursting was detected are denoted in blue and all the other eligible minutes are denoted in red. The minutes in which bursting was identified have lower Re_η, and therefore have smaller η values. The physical explanation for this trend is provided in Section 4.3 along with more findings related to this phenomenon. Results discussed henceforth are of the reconstructed time series of velocity components fluctuations statistics, excluding minutes in which bursting was visually recognized.

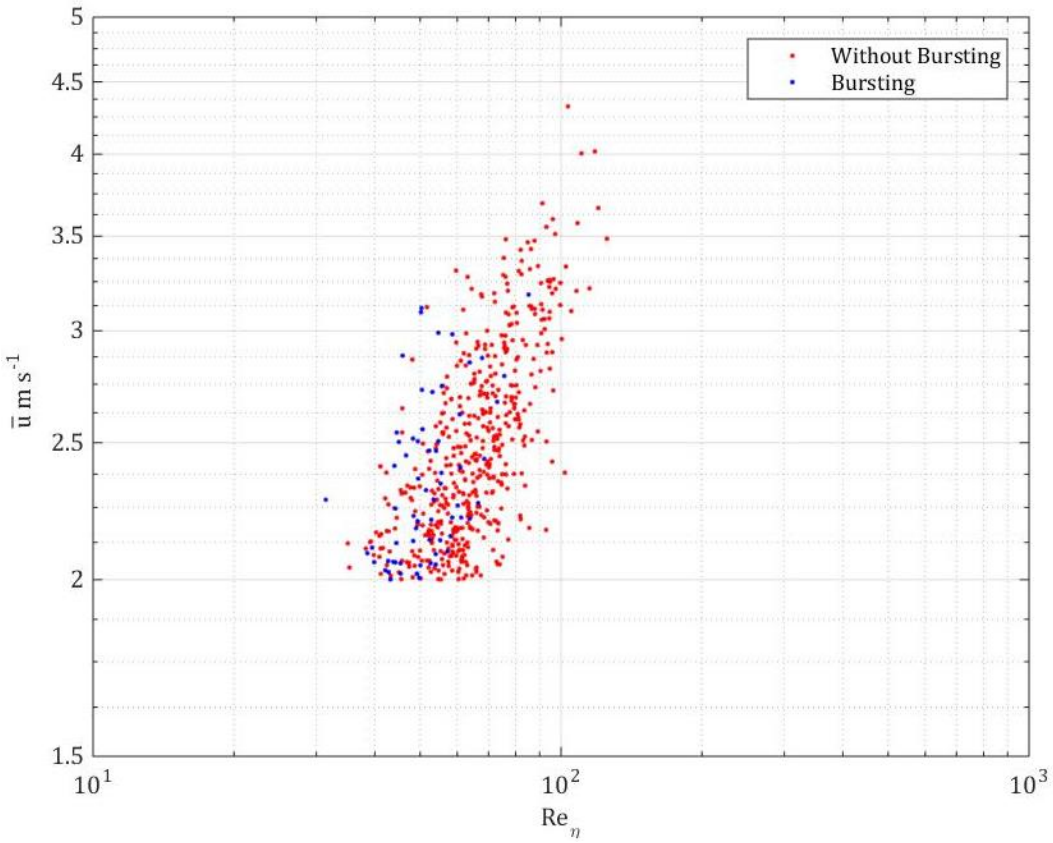

Figure 4.7 Average velocity compared to Reynolds number

The statistics obtained for the main flow velocity component's, u_p, derivative skewness from (1.13) are displayed in Figure 4.8 with respect to their corresponding Re_η. The distribution of velocity derivative skewness values exhibited a significant scatter, indicating the inhomogeneous nature of the turbulence. The calculated values were mostly negative, ranging between -1 and 0, due to the non-Gaussian-probability-density-distribution nature of the perturbations over time. An observed slight increase in skewness values with the increase of explicit *Re* is indeed expected following the

summarized findings in Sreenivasan and Antonia's (1997) study that was based on a large bulk of up to date available field studies (Gibson et al. 1970, Wyngaard and Tennekes 1970, Antonia et al. 1981), lab experiments (Antonia et al. 1982) and numerical models (Jiménez et al. 1993). The skewness values were most commonly found to lie in the range of -0.6 to -0.1 in non-homogeneous flows due to the intermittency of the flow. A linear increase trend line was fitted and found to follow

$$Sk_u = -0.69 + 0.004 Re_\eta \ . \qquad (3.1)$$

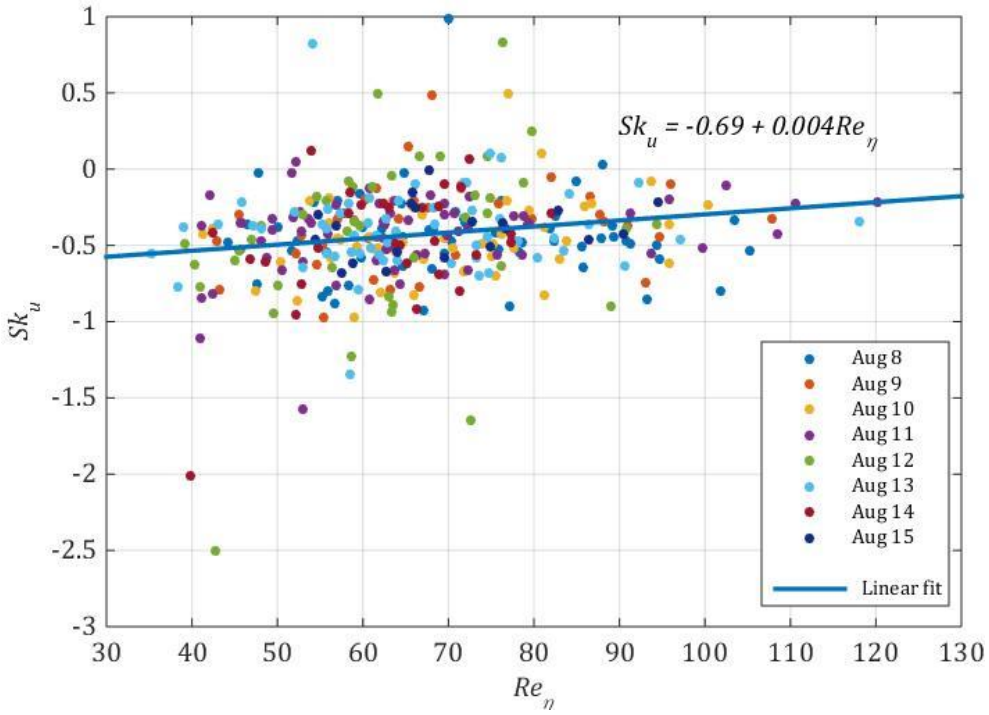

Figure 4.8 Skewness of u_p with respect to Re_η.
Data ensembles from each day are represented with points
in various colors and a linear fit of the data is represented by a solid line.

After, values of TKE and TI were calculated from the time series using equations (1.4-1.5), and are displayed in Figures 4.9 and 4.10. One should bear in mind that the definition of Kolmogorov length scale used in this work are based on the assumption of constant average dissipation rate by definition (Pope 2000). While in fact, as already shown above (Figures 4.5 and 4.6) and is discussed in detail further in the text, the actual dissipation rates obtained from these measurements varied significantly from -5/3 and were not constant through the entire inertial subrange. However, such a definition of explicit Reynolds number allows easy comparison with other results available in literature. Re_η is an implicit value majorly affected by the average velocity, since Kolmogorov scales are $\sim 10^{-4}$ m.

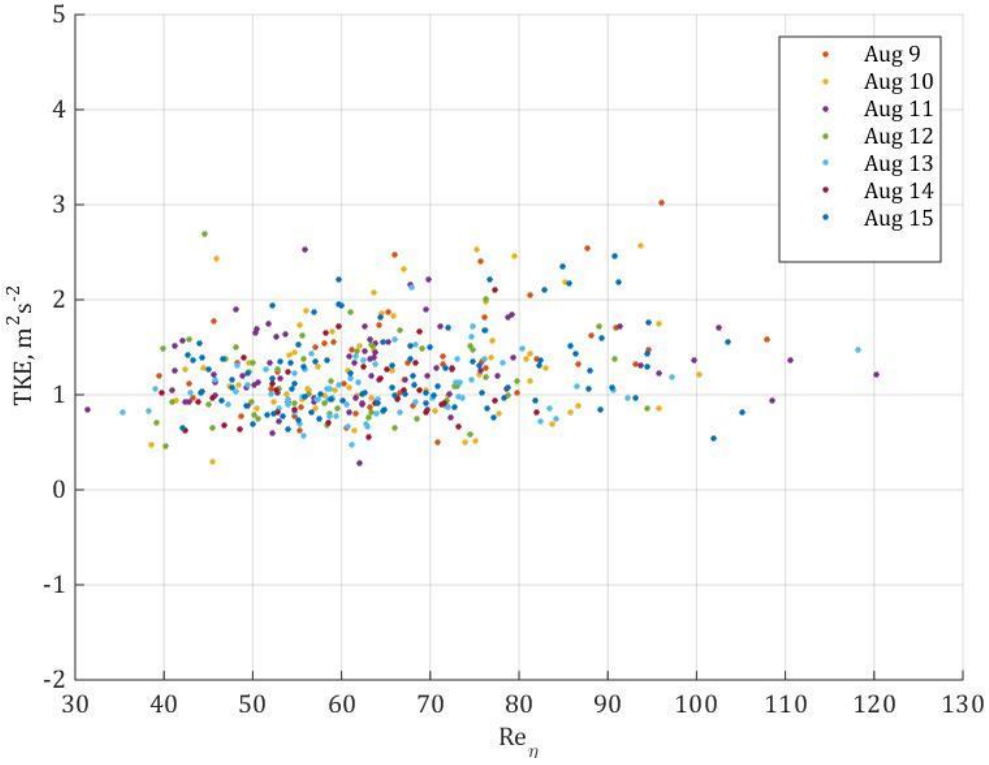

Figure 4.9 TKE with respect to Reynolds number

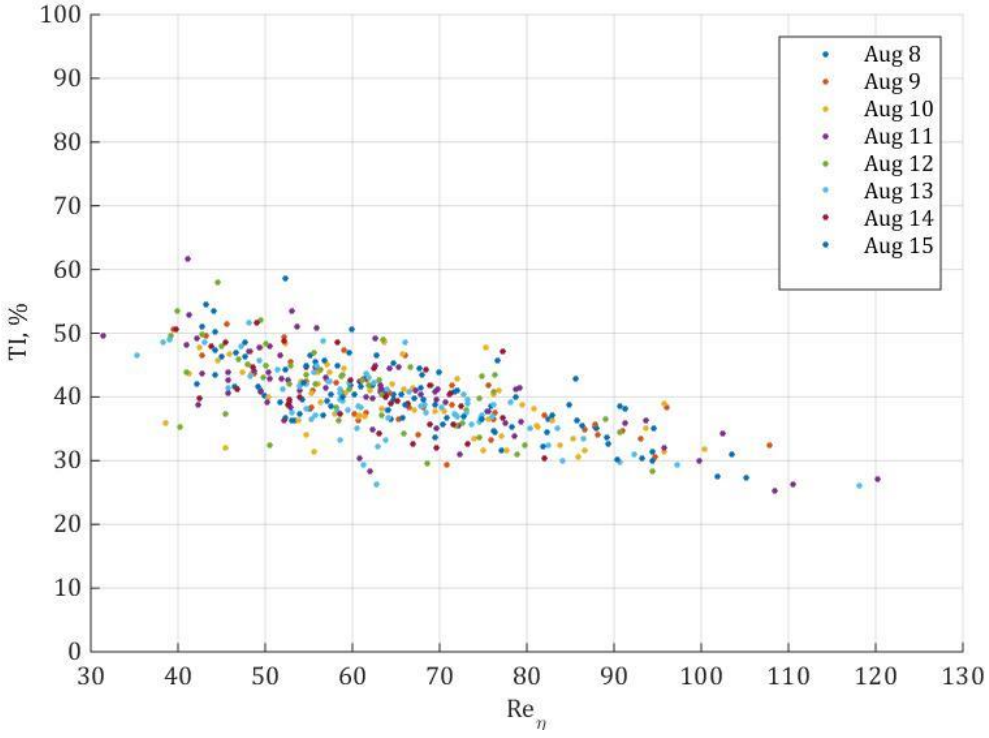

Figure 4.10 TI with respect to Reynolds number

After observing the trends of TKE and TI, the data were averaged over blocks of 5 Re_η values obtaining the empirical fits shown in Figures 4.11 and 4.12. As expected, TKE was found to have a positive correlation with the Re_η, while TI values showed negative correlation with the Re_η, since the rate of change in mean velocity was greater than that of fluctuations' intensity. As Re_η increased, the observed flow became more turbulent and the increase in TKE values was found to follow a linear trend (Figure 4.11) of

$$TKE = 0.87 + 0.004 Re_\eta \ . \qquad (3.2)$$

The reduction in turbulence intensity along the increase in Re_η was also linear and followed the

$$TI = 75 - 0.26 Re_\eta \qquad (3.3)$$

trend.

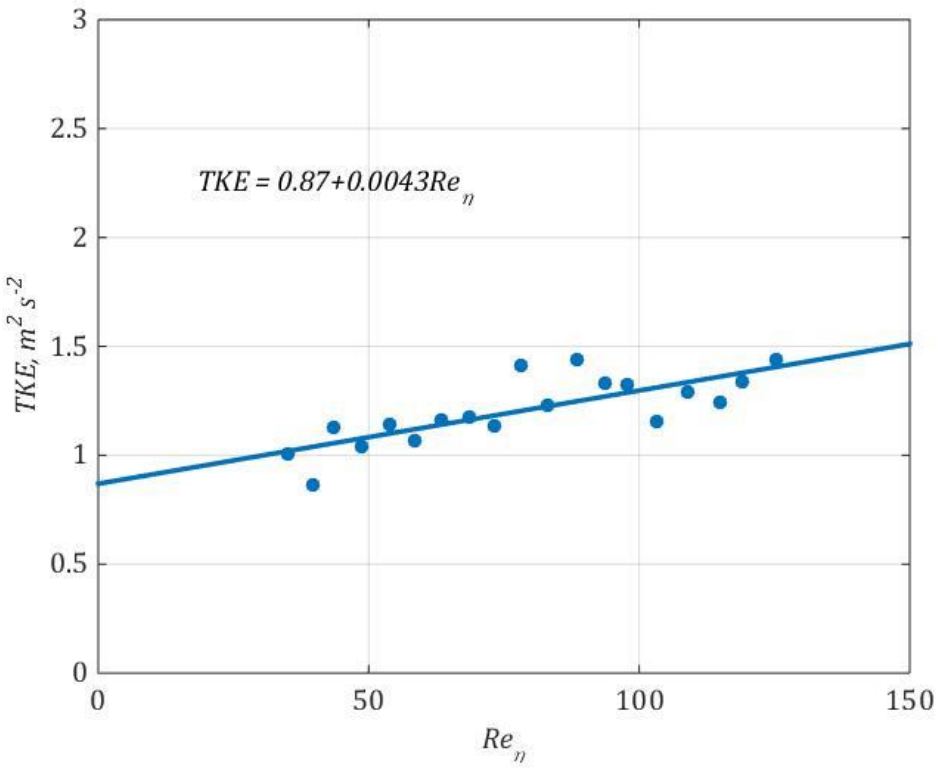

Figure 4.11 Averaged *TKE* as a function of Re_η.

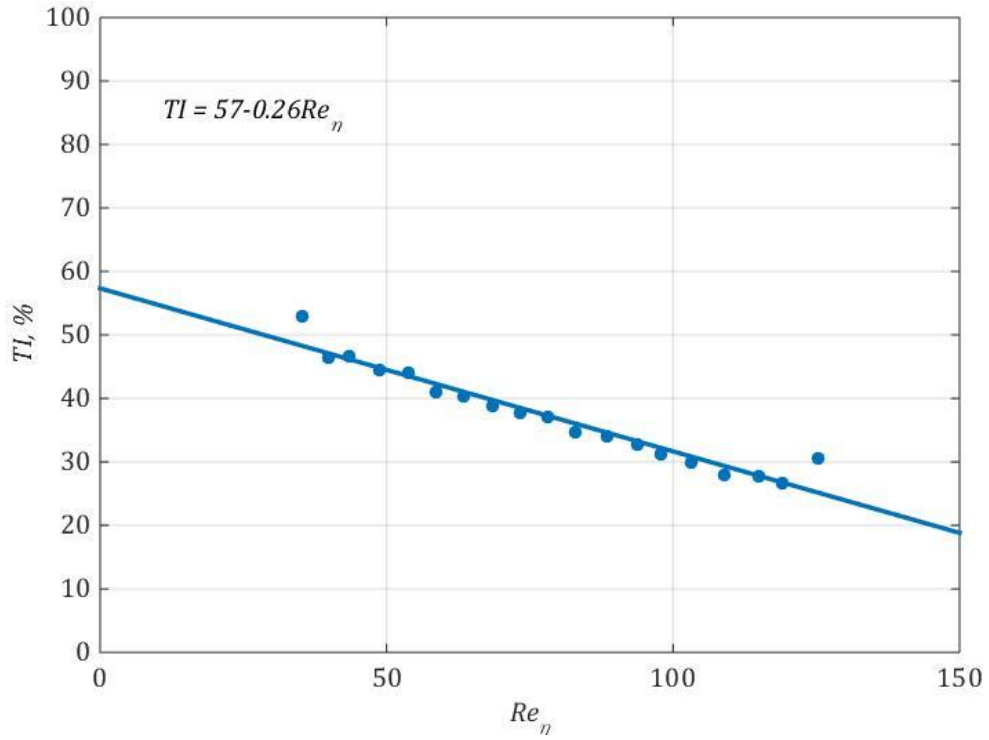

Figure 4.12 Averaged TI as a function of Re_{η}.

The average dissipation rates calculated from the time series using (1.9) are expressed as a function of Re_{η} in Figure 4.13. Scatter of the dissipation values for all measured days exhibits a clear decrease with Re_{η}, but fitting one curve to represent the correlation is not characteristic since the fully solved spectra clearly shows that the dissipation rate was not constant, but changed throughout the inertial subrange. The dissipation rates displayed a rather large scatter. This is, however, expected as these values are the mean representatives for the entire subrange, while the fully resolved spectra showed change of up to 60% in the dissipation rates at some fixed frequency. Instead of presenting 2 average dissipation rates in the inertial subrange, the use of a single representative rate is advantageous for depiction of each minute's turbulence as it provides a consistent scale of comparison among minutes measured here and with other data available in the literature.

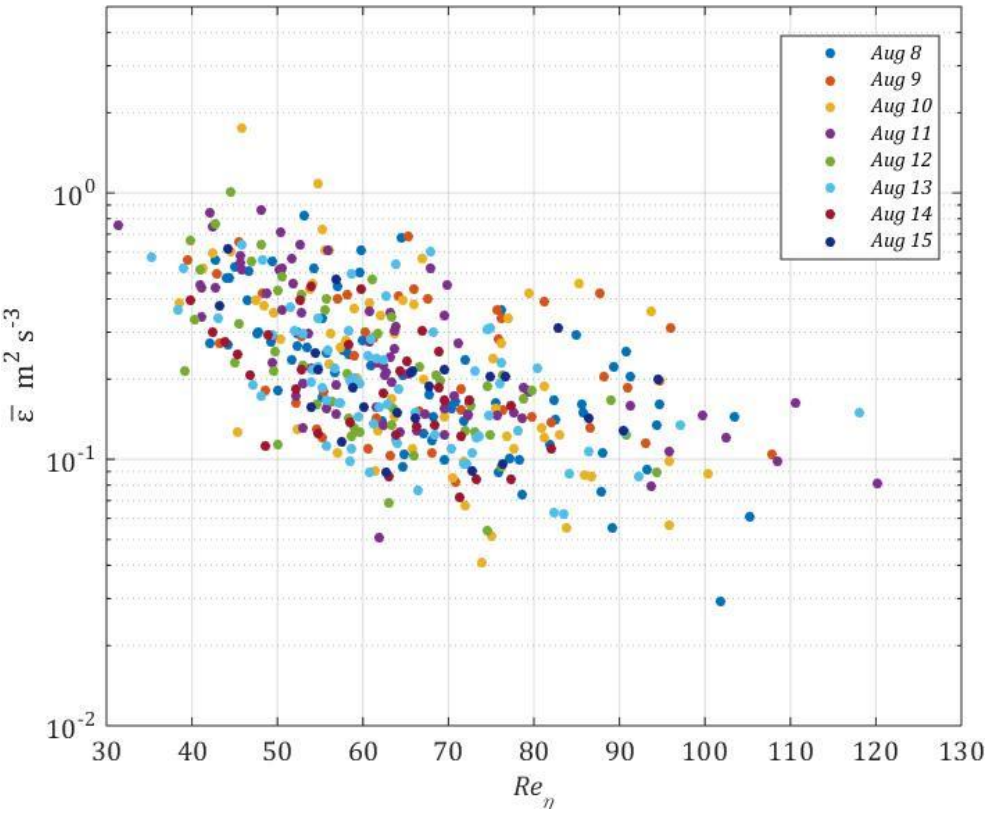

Figure 4.13 Average dissipation rates represented in each day with respect to their explicit Reynolds number.

All of the obtained velocity fluctuations spectra presented rather similar shapes as observed in Figure 4.5. The main similarity was the increase in dissipation rate at higher frequencies range indicating anisotropic turbulence, opposite the often assumed basis for such flows in experiments performed by low resolution instrumentation (e.g. Sonic or LIDAR). Such data allow the spectra to be obtained only for a limited range of low frequencies, and is often fitted by the -5/3 law to derive higher frequency components, while more realistic empirical fits are not available (Kaimal 1978). In the current measurements, the spectra distinctly showed higher average dissipation rates in addition to the change in the dissipation rate occurring at fixed frequencies for each component. The eligible minutes were examined individually and found to follow the same pattern, and in order to confirm the similarity, all eligible minutes' spectra were plotted on one plot all together, yet separately for each component (Figures 4.14-4.16). All of the spectra presented a rather high level of similarity. The slope, representing the rate at which the energy is being transferred down the smaller scales of the turbulence, is the most important feature of the spectrum and spectral data ensembles presented here did form

a tight cloud defining clean slopes in both ranges. The fitted slopes are presented in the plots along with the value of frequency at which average TKE dissipation rate changes, which will be referred to as "transition frequency."

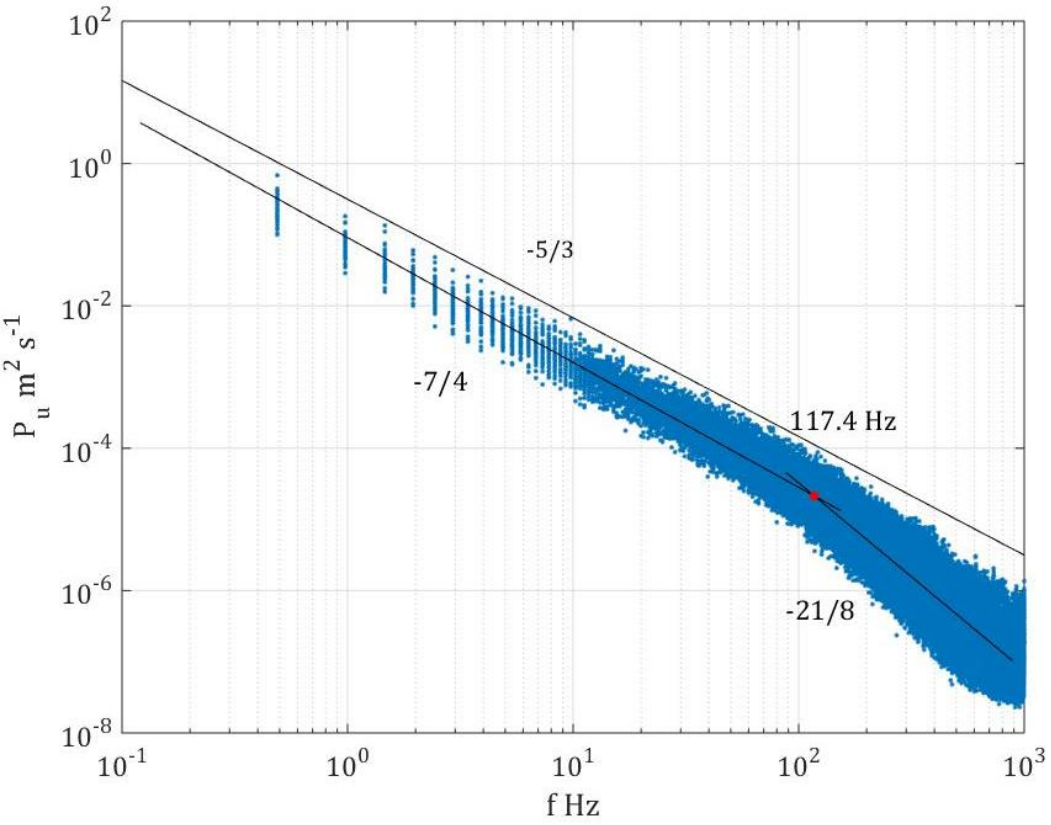

Figure 4.14 The u_p component spectra of all eligible minutes

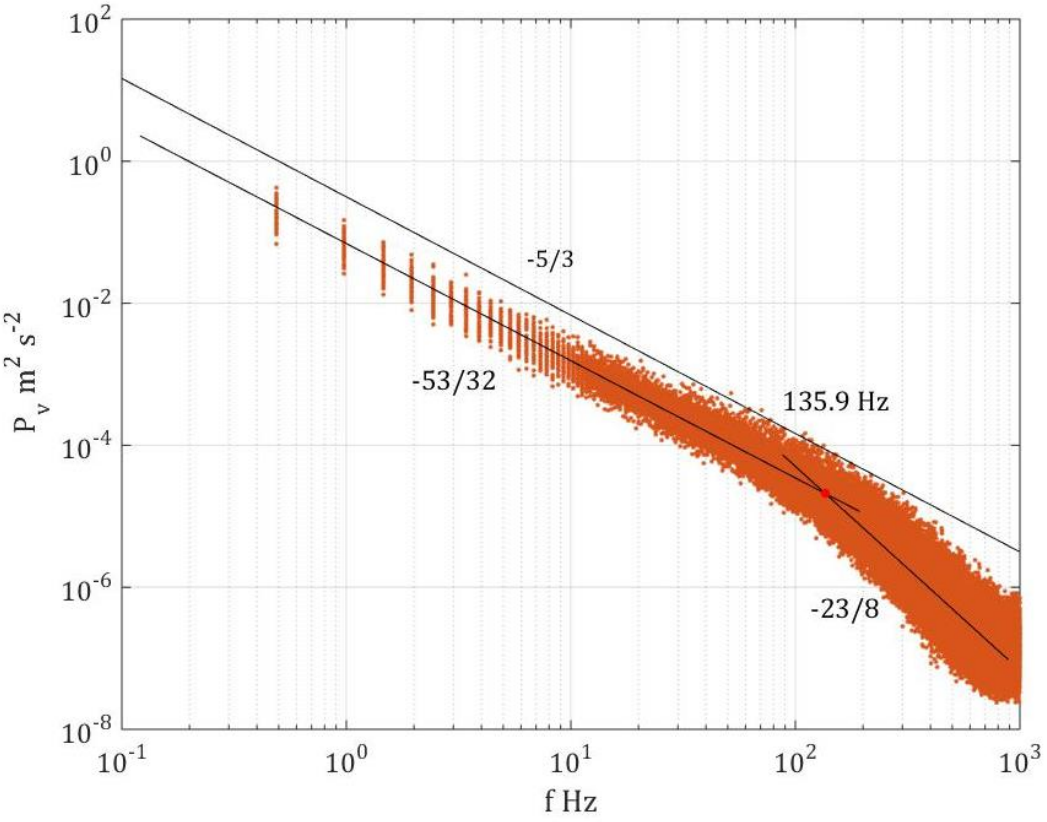

Figure 4.15 The v_p component spectra of all eligible minutes

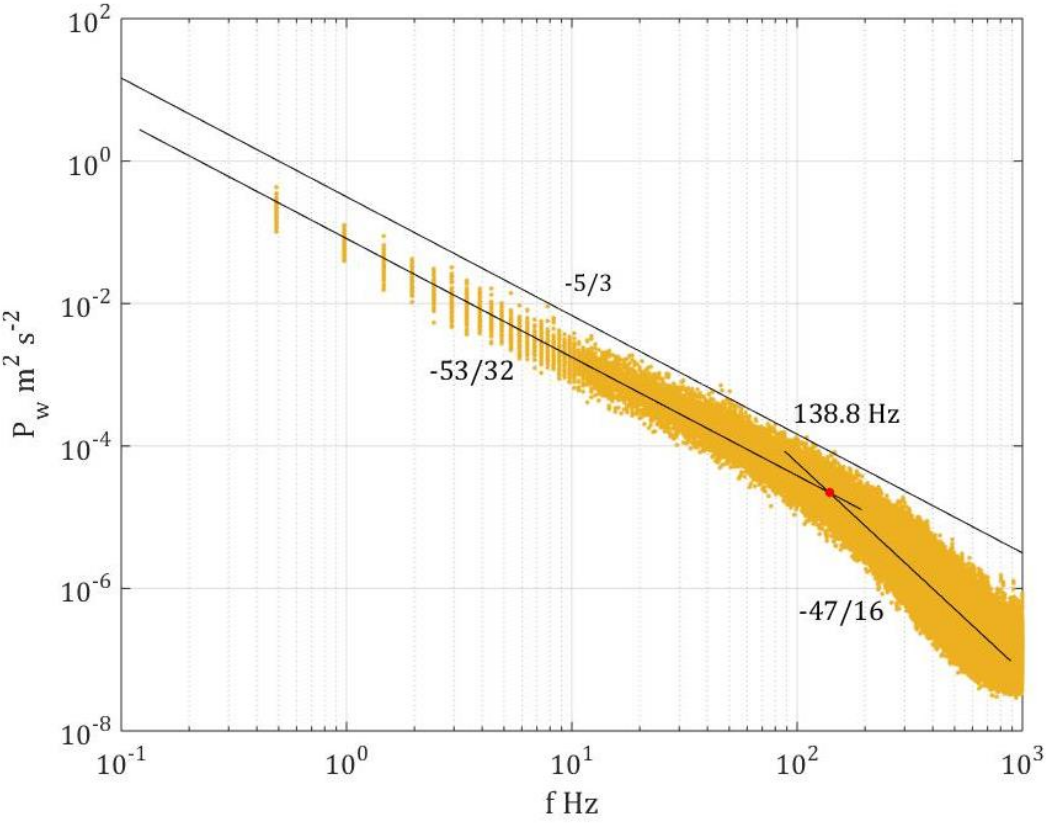

Figure 4.16 The w_p component spectra of all eligible minutes

To assist future researchers in obtaining more accurate spectral results from low resolution measuring devices, a non-dimensional empirical fit to the expected spectral shape of each component was produced. The spectral shapes for the whole ensemble of minute long records without bursting was attained by normalizing the power density using $\lambda \times \overline{u}$, λ being the length of the fly path of the Sonic's sound signal (or the spatial resolution of measuring instrument), and using $\lambda / \overline{u}$ to normalize the frequencies, which eventually produced the normalized non-dimensional power density spectra of velocity fluctuations (Figures 4.17-4.19). Observing similarity, again indicated by the tight clouds defining clear slopes, after normalizing the spectra of all three velocity components, empirical fits (also shown in Figures 4.17-4.19) were produced for each velocity component. The resulting fitted dissipation rates and transition frequency values are also listed in Table 1. These can be used as the more accurate extrapolation basis for each velocity component while performing measurements with only low resolution/slow instruments, and as a useful basis for numerical models.

	u_p	v_p	w_p
First dissipation rate	-1.663	-1.574	-1.579
Second dissipation rate	-2.723	-2.947	-3.029
Transition frequency $\frac{f\lambda}{\overline{u}_s}$	6.402	7.543	7.643

Table 1 Summary of empirical findings:
normalized empirical values of the 2 dissipation rates in the inertial subrange of each velocity component and the "transition frequency" which determines the point of change in dissipation rate.

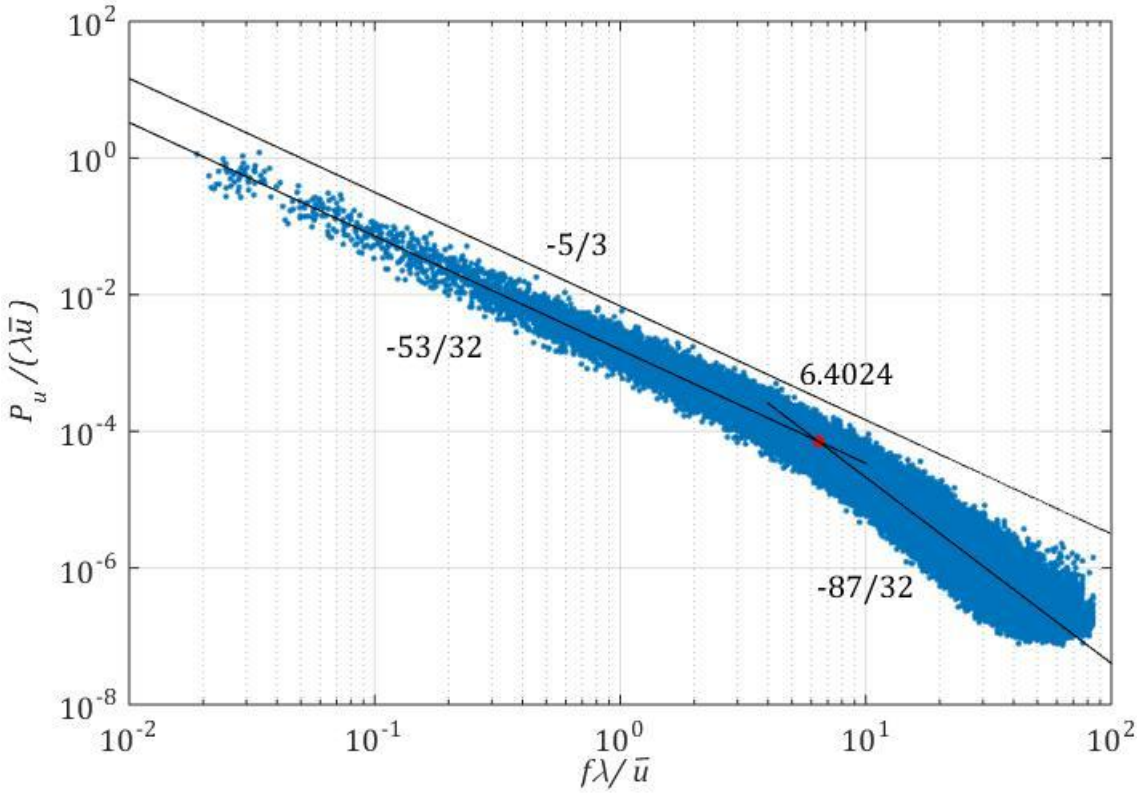

Figure 4.17 Normalized Power Spectra of the u_p Component:

ensemble of all available minute long u_p records and the respective empirical fits.

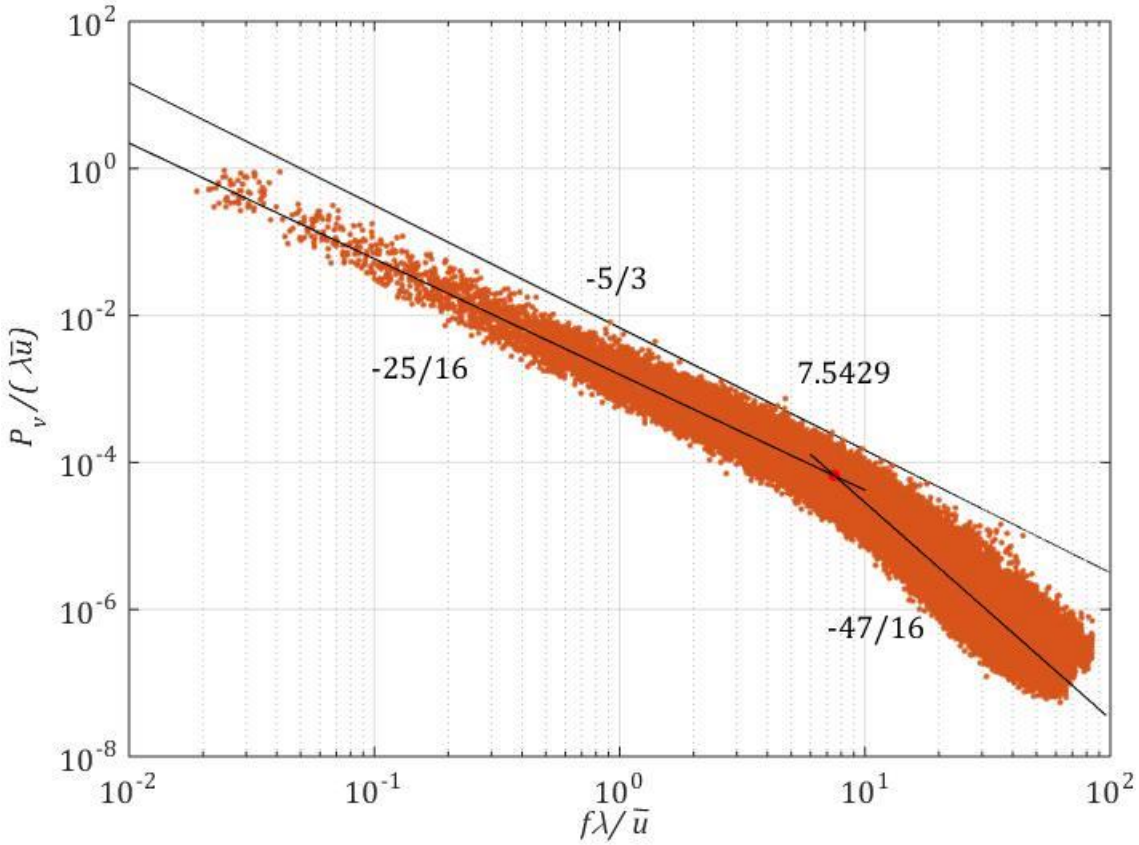

Figure 4.18 Normalized Power Spectra of the v_p Component:
ensemble of all available minute long v_p records and the respective empirical fits.

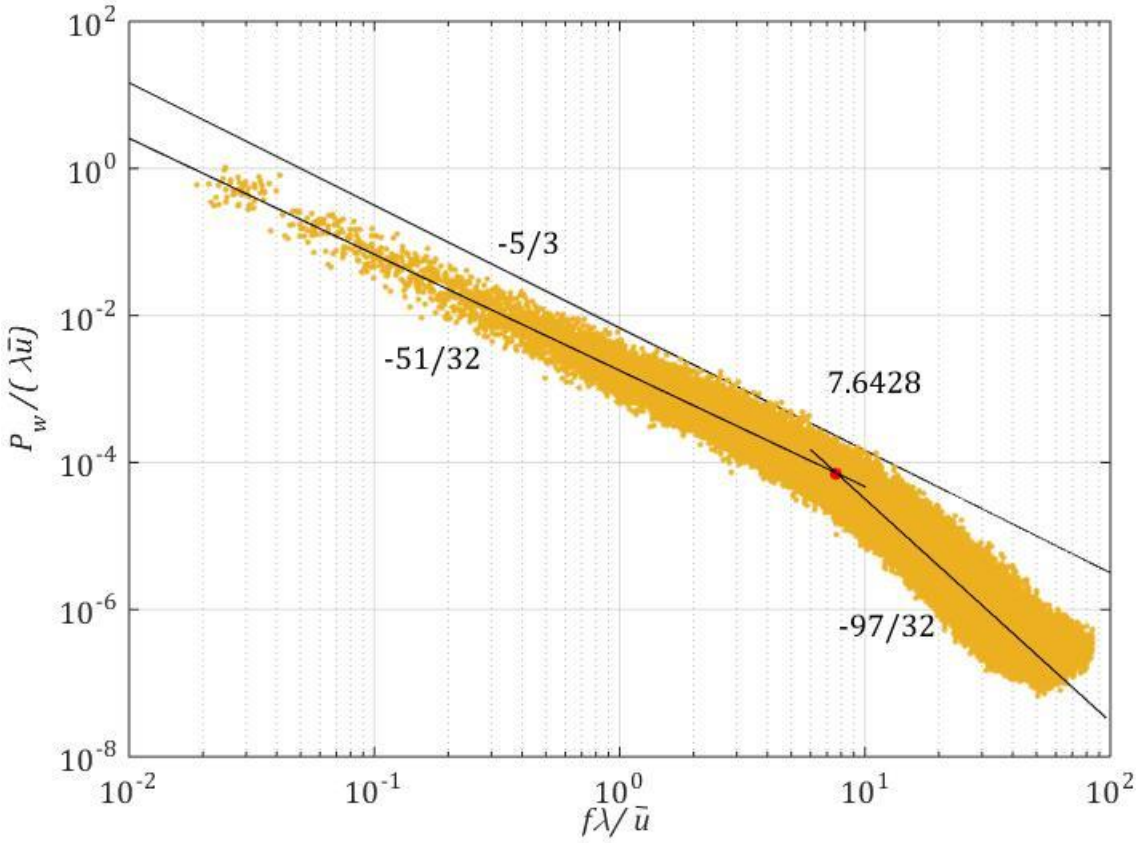

Figure 4.19 Normalized Power Spectra of the w_p Component:
ensemble of all available minute long w_p records and the respective empirical fits.

A repeated trend was found in the normalized spectra, clearly apparent in Table 1. The dissipation rate's transitioning frequency for the mean-flow component u_p was significantly smaller than those of the vertical and horizontal components v_p and w_p, which differ only slightly. Values of dissipation rates at higher frequencies are higher than those at the lower frequency ranges, and increase with each component u, v, and w respectively. Such behavior indicates the non-homogeneity and anisotropy of the turbulence captured in this field study, with the vertical component of the flow being the most dissipative and unstable dimension, which can be attributed to the thermal forcing of the flow. Having in mind future measurements with slow instruments, normalized spectral shapes for non-homogeneous turbulence are therefore presented alongside the derived empirical fits, which will be available for use in future studies.

4.3 The Bursting Phenomenon

The bursting phenomenon is defined as short periods of very high intensity of fluctuations. As previously mentioned, it is extremely difficult to capture in natural setups, but the use of the Combo enabled us to do so in this study. Bursting can be identified in the time series as defined and by examining the spectral shapes and recognizing an increase of fluctuations' energy in a region where normally a constant TKE dissipation rate is observed, seen as "bulges" seen in Figure 4.6. This is explained by injection of energy into the cascade by an external force. Length scales are used to characterize the flow and denote the different points on the spectrum, and considering the differences observed in minutes with and without bursting assists in detecting such injection of energy to the cascade. Initially, in Figure 4.7 the average velocities are plotted against Re_η and minutes with bursting occurrences are distinguished from those without. There, it was concluded that minutes without the bursting occurrences appear to have smaller Re_η at similar $\bar{u}_p$ indicating smaller values of η. The smaller Kolmogorov length scale values carry more energy, due to an addition injected by bursting. Therefore, the viscous forcing terminates the energy cascade at smaller scales.

The same is observed for the Taylor length scale L_T in Figure 4.20. L_T is the length scale indicating the size of eddies at which the viscosity effects are no longer negligible in the cascade of TKE. Finally, the values of horizontal length scale L_H are plotted in Figure 4.21; it is a distribution of horizontal length scale as a function of Re_η, and an increase of L_H is observed with an increase of Re_η. L_H Is the largest length scale represented by the lower frequency range of the spectrum, and represents large eddies through which the energy input occurs in the flow. In bounded turbulent flows, this length scale also represents the height of the BL. Values of L_H of in the entire range of examined minutes is between several meters to tens of meters, reassuring that the Combo was measuring the flow within the boundary layer.

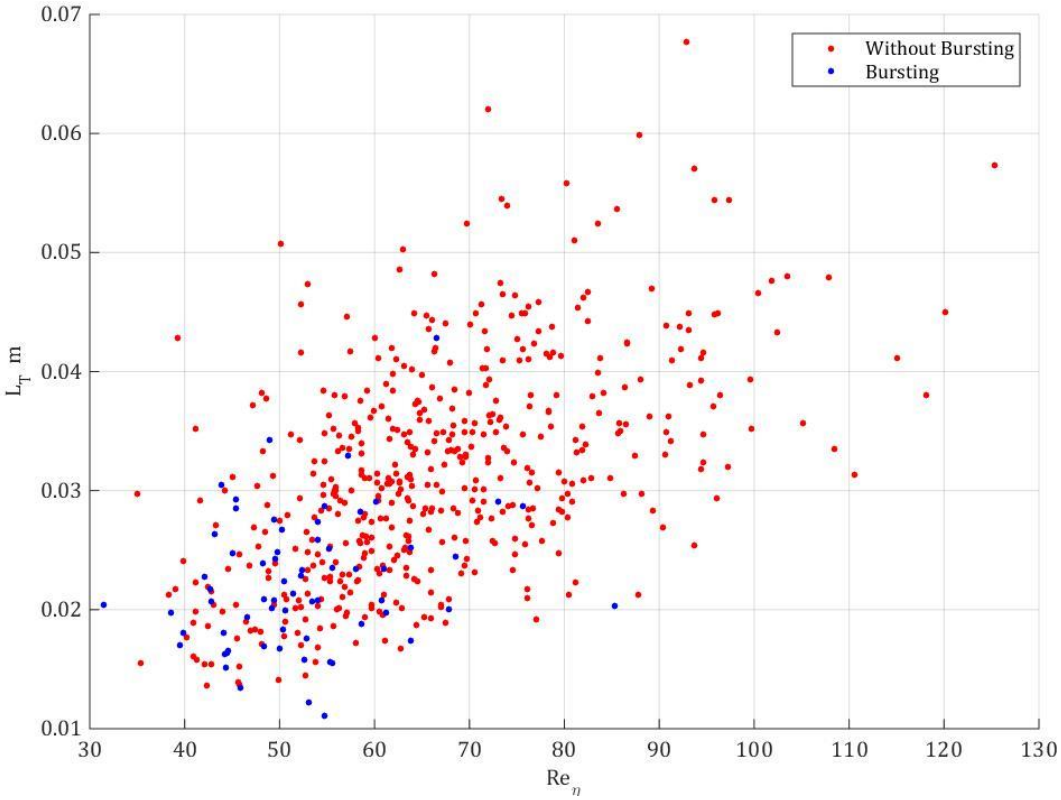

Figure 4.20 Taylor Length Scales

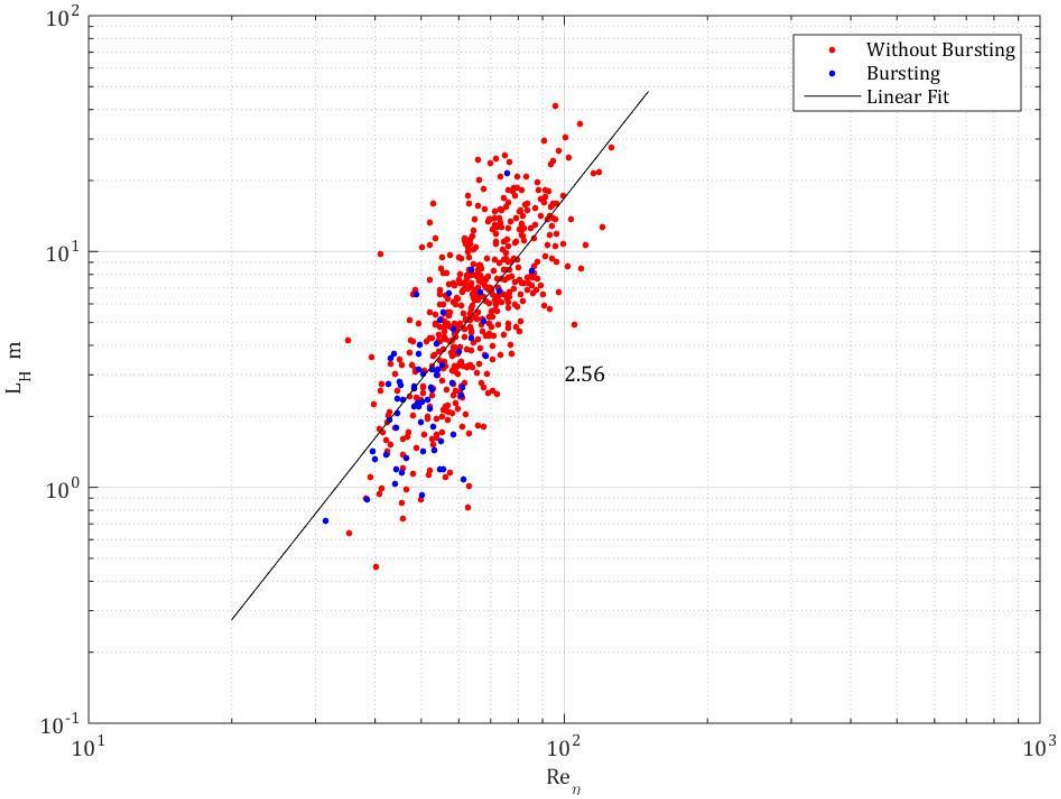

Figure 4.21 Horizontal Length Scales

Figure 4.22 depicts values of L_H, L_T, η obtained from all eligible minutes along the *u* component spectrum. These values are distinguished by minutes in which bursting was present, in blue, to minutes in which it was not, in red; the mean value of each set of datum is denoted on the graph. Interesting features are examined; as expected, the largest length scales correspond to the largest length scales measured by the instrument. The presence of bursting shifts the L_H somewhat to the right indicating energy was input into the cascade at smaller scales. All of the obtained L_T values appear the left of the "transition frequency", though when bursting occurs, the values are closer to the breaking frequency pointing towards an increase in homogeneity of the flow as more mixing is introduced into the flow by the bursting events. A similar trend is observed in the Kolmogorov length scale, the values calculated for minutes that include bursting are somewhat smaller, and since smaller scales carry more energy that is injected to them by bursting, the viscous effects are capable of terminating the energy cascade only at smaller scales.

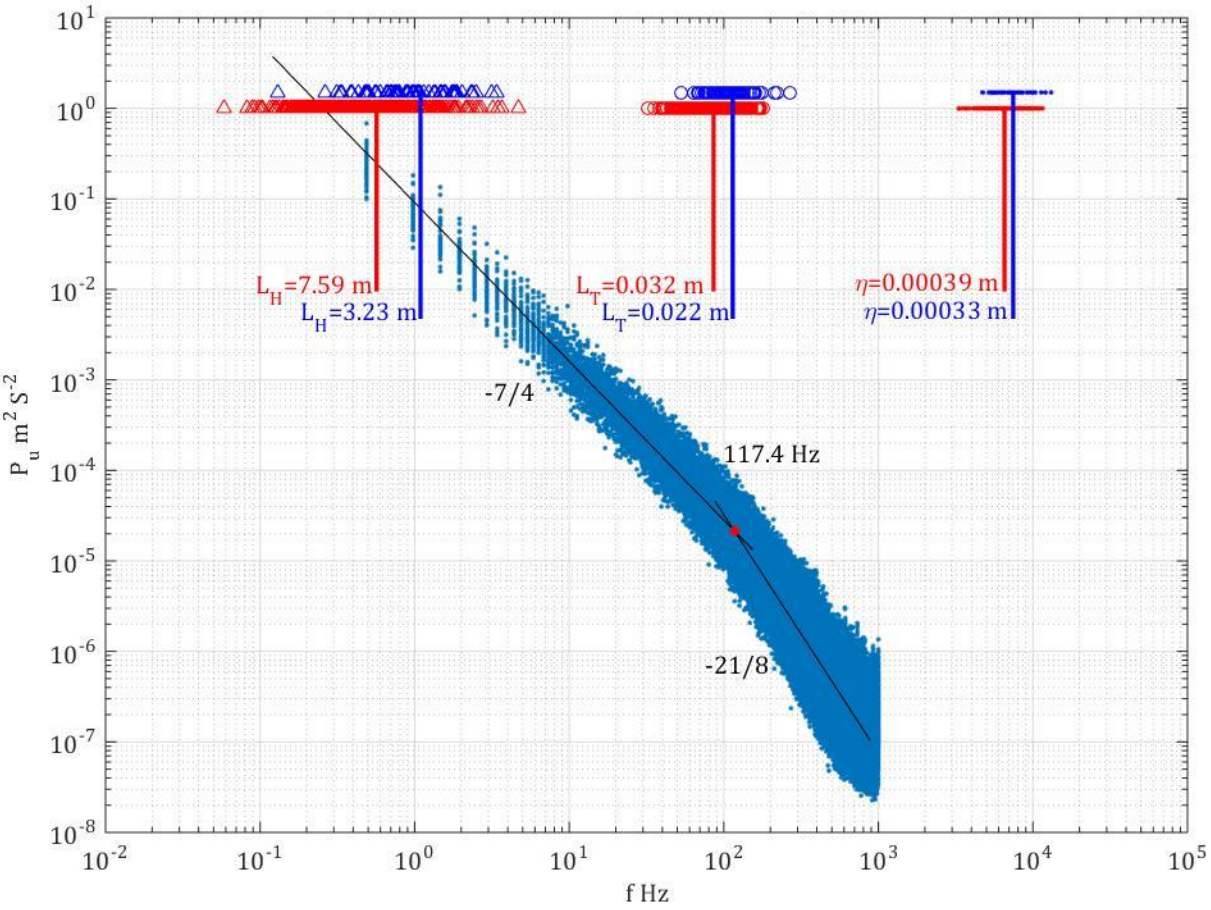

Figure 4.22 Length scales on the *u* component spectrum for perspective

The identification of the mechanism responsible for the bursting phenomenon was proposed earlier as the injection of energy from an external force; it is now necessary to confirm it. Thermally driven flow was initiated by unstable stratification, warmer air stratified below the cooler air. This caused the warmer air to rise, steering the flow and eventually creating anabatic BL flow. Sometimes, overly heated bulges of air manage to perform rapid climbs and suddenly find themselves in a cooler flow above. These bulges carry more kinetic energy that they eject into the flow in the location of intrusion, causing rapid mixing and increased fluctuations. This suggested mechanism was confirmed by examining the frequency of occurrences of bursting and comparing them to the normalized mean velocity curve (Figure 4.23) and to the normalized temperature gradient distribution (Figure 4.24). The bursting occurrences frequencies are presented here in a percentile scale. The frequency of bursting occurrence significantly increases as the unstable stratification starts to increase, also accompanied by an increase in average velocity. In other terms, the higher the temperature gradient is, the more are the chances of hot bulges of air to perform intrusion into higher altitude consisting of cooler air mass, effectively triggering bursting.

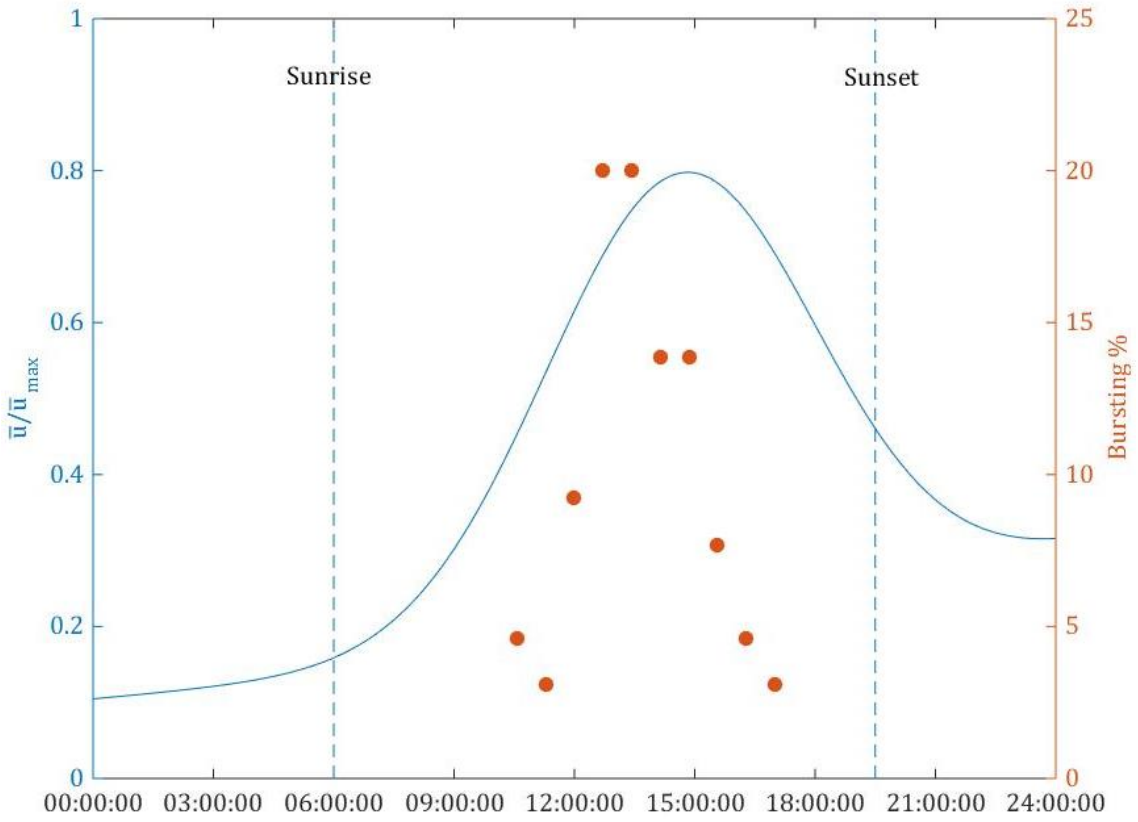

Figure 4.23 Normalized average velocity curve and frequency of bursting appearance

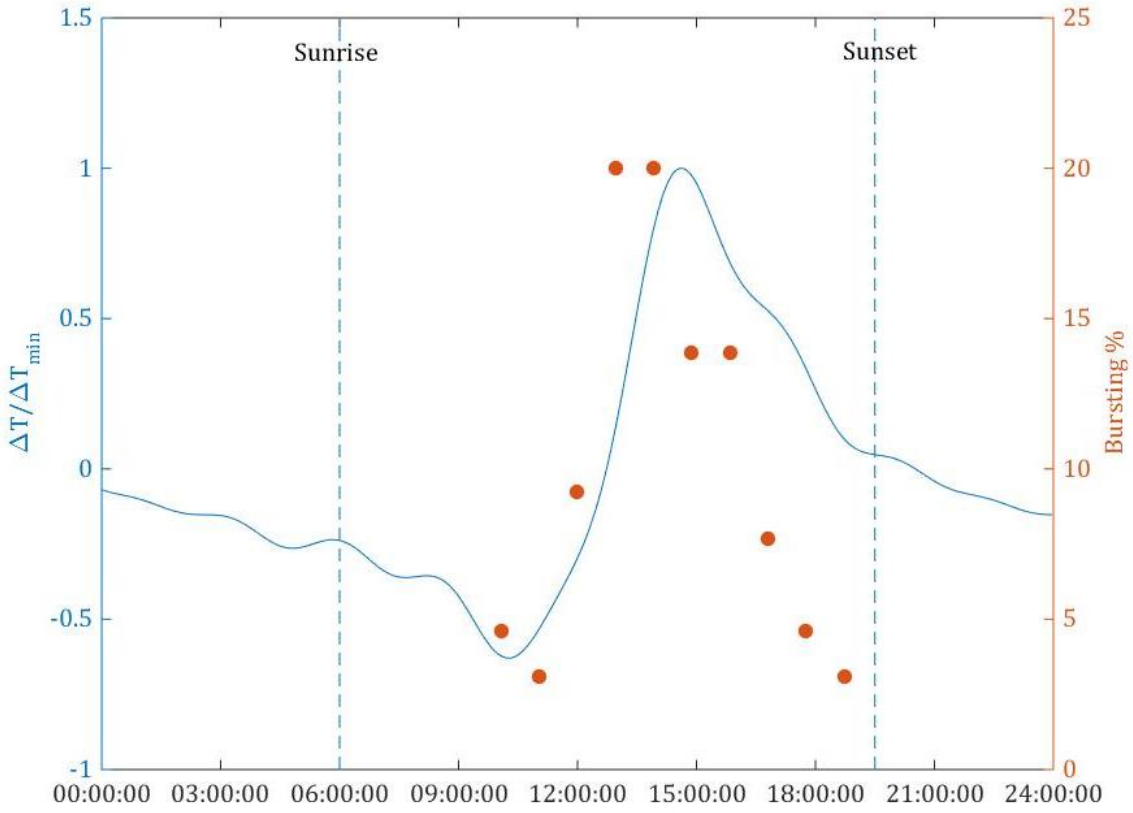

Figure 4.24 Normalized temperature gradients curve and frequency of bursting appearance

Another method that was used in this study to further confirm the proposed mechanism of bursting being triggered by the intruding bulges of warm air into the much cooler flow and swiftly injecting energy into the cascade, was by observation of the spectral shapes. The bursting phenomenon was explained to appear in the spectra by the transition to a higher dissipation rate characterized by a large "bulge" (Figure 4.6b, d), the so called "bottleneck" effect (Falkovich 1994, Saddoughi and Veeravalli 1994, Tatarskii 2005) that was previously mentioned.

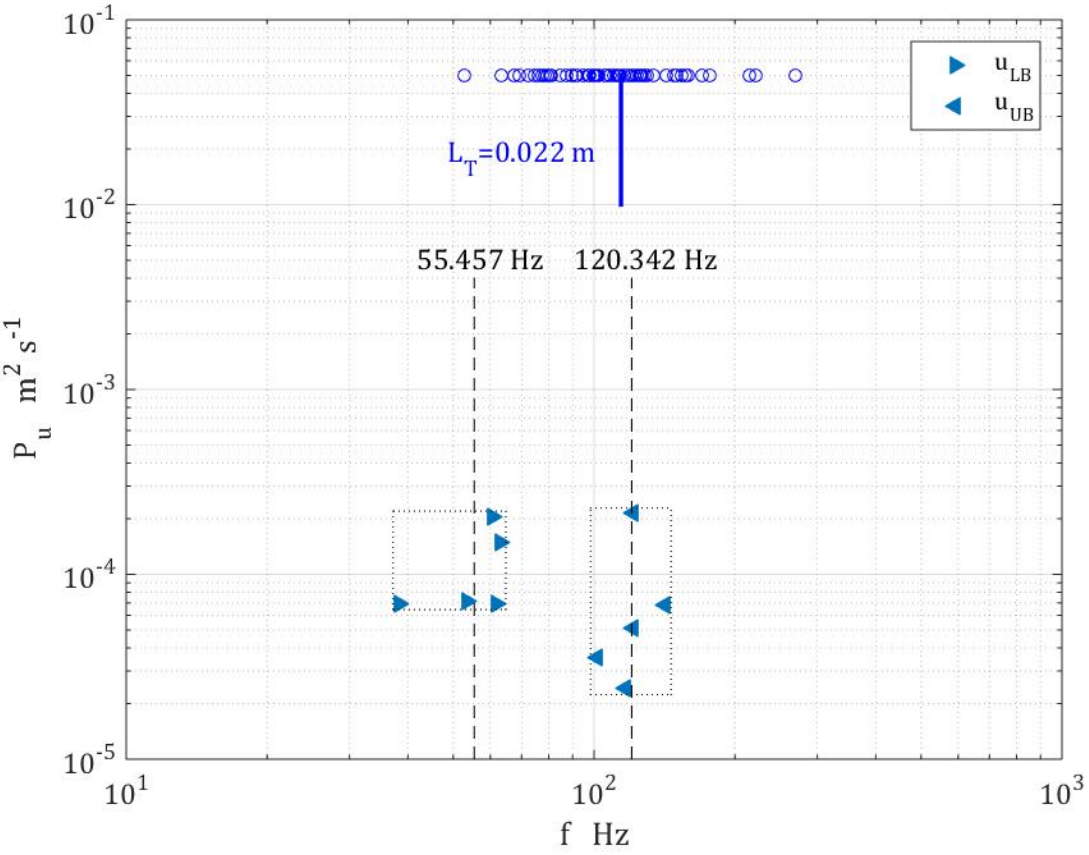

Figure 4.25 Spectral identification of u_p component

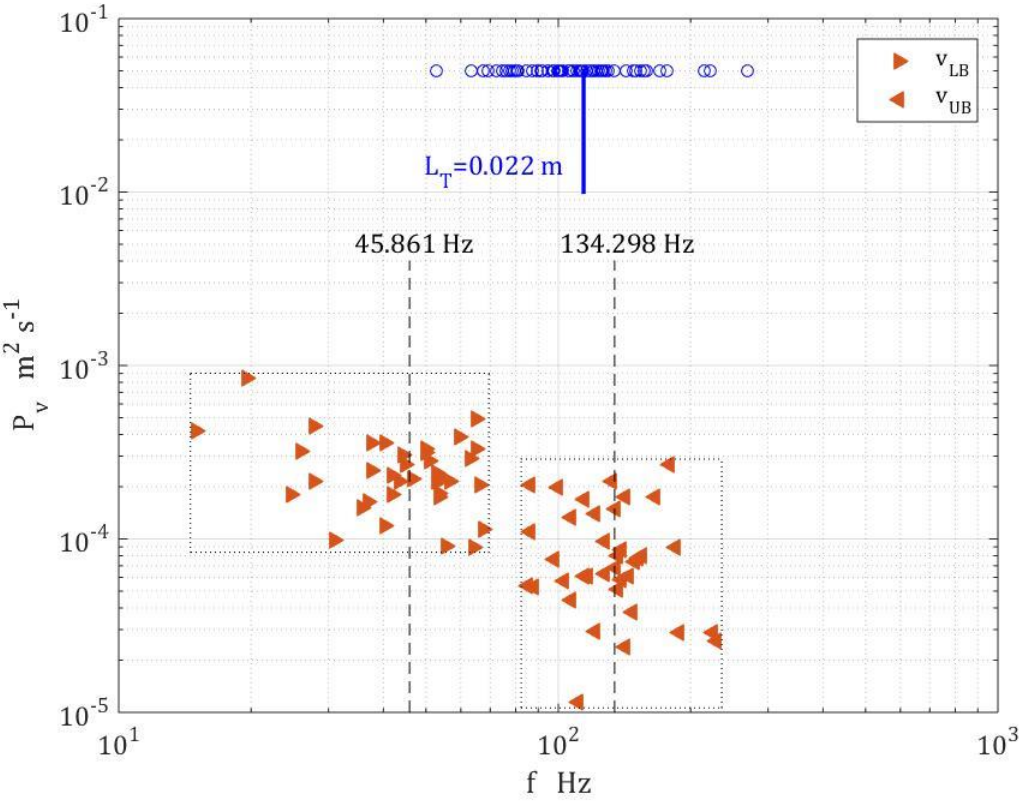

Figure 4.26 Spectral identification of v_p component

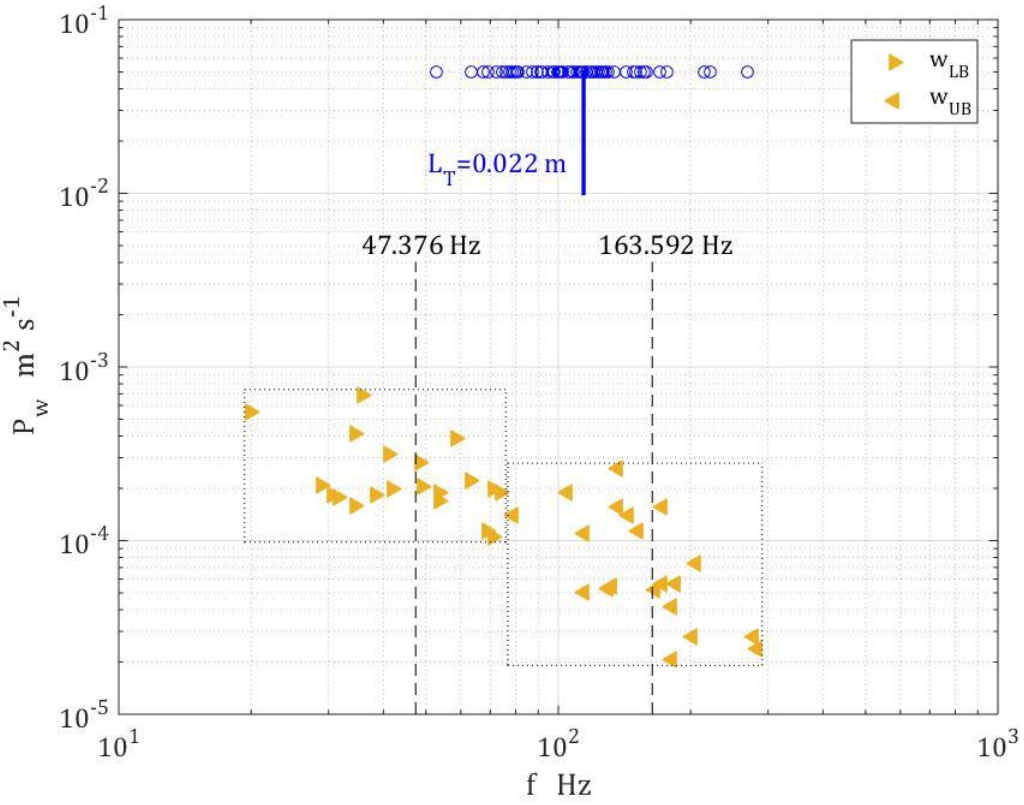

Figure 4.27 Spectral identification of w_p component

The bottleneck is present in the spectral shapes of all velocity field components, but was mostly pronounced in *v* and *w* components. Figures 4.25-4.27 demonstrate the bottleneck ranges of each component in which both starting and ending boundaries of the increase in $\bar{\varepsilon}$ were clearly identified on the spectrum. The lower and upper bounds were visually identified on each spectrum and their location was recorded, while the plots in which the bulge's boundaries were less clear were excluded. The L_T values of minutes in which bursting was identified are also plotted in each of those figures to determine whether or not viscous forces were present and dominant in the generation of the bursting events. The bottleneck ranges begin at frequencies lower than the transition frequency and the range of L_T values indicating bursting's originated disturbances were free of dominant viscous forces, rendering that the viscous forces are not a part of the generation mechanism for these bursting occurrences. This further confirms that the assumption for the generation mechanism is correct as the length scale of heated bulges of heat are expected to be larger than that of Taylor's length scale.

Chapter 5 Conclusions

Thermally driven turbulent flows are common in the atmospheric BL, especially in anabatic/katabatic forms, and greatly influence microclimates. Such flows are considered irregular, chaotic and unpredictable, and therefore statistical analyses are used to characterize them. Various turbulence statistics that would assist in weather and climate predictions/modeling could be obtained to further characterize the observed anabatic BL flow, including the fully resolved spectra of velocity fluctuations. However, it is difficult to capture the fine scales of such flows with the traditional outdoors measuring instrumentation due to the flow's unstable conditions and sometimes harsh conditions in the field. In this particular work, the use of a Combo probe, consisting of collocated hot-film and Sonic anemometers, was made to obtain comprehensive records of fine scale turbulence during several days of continuous measurements in the field. Implementing the NN based *in-situ* calibration method established in Kit et al. (2010), continuous measurements of naturally developing thermally driven anabatic flow were performed at a moderate slope located in northern Israel. Successfully tapping into the smallest scales of the local turbulent boundary-layer flow alongside obtaining records of the mean-flow magnitude and direction fluctuations during the 8 days of the experiment, a clear diurnal pattern associated with the heating cycle was detected and analyzed. After confirming the thermally driven nature of the examined anabatic BL, given the aforementioned results and diurnal inclinations, the turbulence statistics of the flow were obtained and examined in detail. The main findings are summarized as follows:

a. Development of a moderately unstable anabatic flow was detected, strongly correlated with the local temperature gradient development due to solar heating of the slope. The flow was characterized by implicit, Kolmogorov length scale based, Re_η values in the range between 30 and 130.
b. The turbulence intensity was found to decrease with the increase of mean velocity, accompanied by the increase of the TKE of the flow field, both exhibiting a linear dependency on Re_η. Calculated values of velocity-derivative skewness of the main flow direction component were mostly negative, in the range between -1 and 0, also showing linear increase as a function of Re_η. Respective empirical fits for *TI, TKE* and Sk_u were derived and presented.

c. Fully resolved spectra of all three-velocity-field components were obtained, revealing the presence of bursting in approximately 15% of the time.
d. Examination of the spectral shapes revealed strong similarity for all times at which the flow was judged to be unidirectional up-the-slope, excluding the minutes in which bursting was detected. The energy dissipation rates were found not to be constant, but to increase at fixed values of frequency for each velocity field component. The lowest transition frequency was detected in the velocity component along the mean direction of the flow, while those of the horizontal and vertical components were somewhat higher and similar. A normalization of velocity fluctuations energy density spectra was proposed based on the parameters of the slow Sonic anemometer. These were fitted with empirical curves.
e. Examination of minutes in which the bursting was detected was done separately. After examining the length scales of bursting minutes and comparing them to those without the presence of bursting, it was indicated that the bursting occurrences made the flow appear to be more homogeneous due to the intense mixing motions. Spectral identification of bursting was marked by a local increase in $\overline{\varepsilon}$ at specific ranges of frequencies. The ranges began at values lower than L_T, indicating bursting originated disturbances/fluctuations are mostly free of viscosity influences.
f. A generation mechanism for the bursting that appeared in this flow was suggested, examined, and confirmed. Rapid raise of bulges of heated air intruded into cooler portion of the flow causing instabilities expressed as the intense mixing motions were found to be responsible.

The derived empirical fits and especially those of the spectral shapes, valid within the limitations imposed by the presented experimental conditions, offer a useful base for producing more accurate future measurements using only low-spatial/temporal resolution instrumentation and for numerical modelling of turbulent flows developing in mountainous terrain.

Chapter 6 References

Antonia R, Satyaprakash B, Chambers A (1981) Reynolds number dependence of high-order moments of the streamwise turbulent velocity derivative. Bound Layer Meteorol 21:159–171.

Antonia R, Satyaprakash B, Hussain A (1982) Statistics of fine-scale velocity in turbulent plane and circular jets. J Fluid Mech 119:55–89. doi: 10.1017/S0022112082001268

Bruun HH (1995) Hot wire anemometry : principles and signal analysis. Oxford University Press

Choi W, Faloona IC, McKay M, et al (2011) Estimating the atmospheric boundary layer height over sloped, forested terrain from surface spectral analysis during BEARPEX. Atmos Chem Phys 11:6837–6853. doi: 10.5194/acp-11-6837-2011

Davidson PA (2004) Turbulence: an introduction for scientists and engineers. Oxford University Press

Demko JC, Geerts B, Miao Q, Zehnder JA (2009) Boundary Layer Energy Transport and Cumulus Development over a Heated Mountain: An Observational Study. Am Meteorol Soc Mon Weather Rev 137:447–468. doi: 10.1175/2008MWR2467.1

Ellis AW, Hilderbrandt ML, Thomas WM, Fernando HJS (2000) Analysis of the climatic mechanism contributing to the summertime transport of lower atmospheric ozone across metropolitan Phoenix, Arizona, USA. Clim Res 15:13–31. doi: 10.3354/cr015013

Falkovich G (1994) Bottleneck phenomenon in developed turbulence. Phys Fluids 6:1411–1414. doi: 10.1063/1.868255

Faller AJ (1965) Large Eddies in the Atmospheric Boundary Layer and Their Possible Role in the Formation of Cloud Rows. J Atmos Sci 22:176–184.

Fedorovich E, Shapiro A (2009) Structure of numerically simulated katabatic and anabatic flows along steep slopes. Acta Geophys 57:981–1010. doi: 10.2478/s11600-009-0027-4

Fernando HJS (2010) Fluid Dynamics of Urban Atmospheres in Complex Terrain. Annu Rev Fluid Mech 42:365–389. doi: 10.1146/annurev-fluid-121108-145459

Fernando HJS, Lee SM, Anderson J, et al (2001) Urban Fluid Mechanics: Air Circulation and Contaminant Dispersion in Cities. Environ Fluid Mech 1:107–164. doi: 10.1023/A:1011504001479

Fernando HJS, Pardyjak ER, Di Sabatino S, et al (2015) The materhorn : Unraveling the intricacies of mountain weather. Bull Am Meteorol Soc 96:1945–1968. doi: 10.1175/BAMS-D-13-00131.1

Gibson CH, Stegen GR, Williams RB (1970) Statistics of the fine structure of turbulent velocity and temperature fields measured at high Reynolds number. J Fluid Mech 41:153–167. doi: 10.1017/S0022112070000551

Hayashi T (1994) An analysis of wind velocity fluctuations in the atmospheric surface layer using an orthogonal wavelet transform. Bound Layer Meteorol 70:307–326.

Hocut CM, Liberzon D, Fernando HJS (2015) Separation of upslope flow over a uniform slope. J Fluid Mech 775:266–287. doi: 10.1017/jfm.2015.298

Hunt JCR, Fernando HJS, Princevac M (2003) Unsteady Thermally Driven Flows on Gentle Slopes. J Atmos Sci 60:2169–2182. doi: 10.1175/1520-0469(2003)060<2169:UTDFOG>2.0.CO;2

Jiménez J, Wray A a., Saffman PG, Rogallo RS (1993) The structure of intense vorticity in isotropic turbulence. J Fluid Mech 255:65–90. doi: 10.1017/S0022112093002393

Kaimal J. (1978) Sonic Anemometer Measurement of Atmospheric Turbulence. In: Proceedings of the Dynamic Flow Conference 1978. pp 551–565

Kaimal JC, Finnigan JJ (1994) Atmospheric boundary layer flows: their structure and measurement. New York

Kim H, Kline S, Reynolds W (1971) The production of turbulence near a smooth wall i n a turbulent boundary layer. J Fluid Mech 50:133–160.

Kit E, Cherkassky A, Sant T, Fernando HJS (2010) In Situ Calibration of Hot-Film Probes Using a Collocated Sonic Anemometer: Implementation of a Neural Network. J Atmos Ocean Technol 27:23–41. doi: 10.1175/2009JTECHA1320.1

Kit E, Hocut C, Liberzon D, Fernando H (2016) Fine-Scale Turbulent Bursts in Stable Atmospheric Boundary Layer in Complex Terrain.

Kit E, Liberzon D (2016) 3D-calibration of three- and four-sensor hot-film probes based on collocated sonic using neural networks. Meas Sci Technol 27:20. doi: 10.1088/0957-0233/27/9/095901

Kolmogorov AN (1941) The Local Structure of Turbulence in Incompressible Viscous Fluid for Very Large Reynolds Numbers. Proc Acad Sci USSR, Geochemistry Sect 30:299–303. doi: 10.1098/rspa.1991.0075

Krishnamurthy R, Calhoun R, Billings B, Doyle J (2011) Wind turbulence estimates in a valley by coherent Doppler lidar. Meteorol Appl 18:361–371. doi: 10.1002/met.263

Lothon M, Lenschow DH, Mayor SD (2009) Doppler lidar measurements of vertical velocity spectra in the convective planetary boundary layer. Boundary-Layer Meteorol 132:205–226. doi: 10.1007/s10546-009-9398-y

Lumley JL (1965) Interpretation of Time Spectra Measured in High-Intensity Shear Flows. Phys Fluids 8:1056. doi: 10.1063/1.1761355

McNaughton K, Laubach J (2000) Power spectra and cospectra for wind and scalars in a disturbed surface layer at the base of an advective inversion. Boundary-layer Meteorol 96:143–185. doi: 10.1023/A:1002477120507

Monti P, Fernando HJS, Princevac M, et al (2002) Observations of Flow and Turbulence in the Nocturnal Boundary Layer over a Slope. J Atmos Sci 59:2513–2534. doi: 10.1175/1520-0469(2002)059<2513:OOFATI>2.0.CO;2

Narahari Rao K, Narasimha R, Badri Narayanan M (1971) The “bursting” phenomenon in a turbulent boundary layer. J Fluid Mech 48:339–352.

Noppel H, Fiedler F (2002) Mesoscale heat transport over complex terrain by slope winds- a conceptual model and numerical simulations. Boundary-Layer Meteorol 104 104:73–97.

Oncley SP, Friehe CA, Larue JC, et al (1996) Surface Layer Fluxes Profiles and Turbulence Measurements over Uniform Terrain under Near Neutral Conditions. J Atmos Sci 53:1029–1044.

Otarola S, Dimitrova R, Leo L, et al (2016) On the role of the Andes on weather patterns and related environmental hazards in Chile. In: AMS January 2016.

Pope SB (2000) Turbulent flows. Cambridge University Press, New York

Potter H, Graber HC, Williams NJ, et al (2015) In situ Measurements of Momentum Fluxes in Typhoons. J Atmos Sci 72:104–118. doi: 10.1175/JAS-D-14-0025.1

Princevac M, Fernando HJS (2007) A criterion for the generation of turbulent anabatic flows. Phys Fluids

19:1051021–1051027. doi: 10.1063/1.2775932

Rampanelli G, Zardi D, Rotunno R (2004) Mechanisms of Up-Valley Winds. J Atmos Sci 61:3097–3111. doi: 10.1175/JAS-3354.1

Reuten C, Steyn DG, Allen SE (2007) Water tank studies of atmospheric boundary layer structure and air pollution transport in upslope flow systems. J Geophys Res Atmos 112:1–17. doi: 10.1029/2006JD008045

Saddoughi SG, Veeravalli and S V. (1994) Local isotropy in turbulent boundary layers at high Reynolds number. J Fluid Mech 268:333–372. doi: 10.1017/S0022112094001370

Schumann U (1990) Large-eddy simulation of the up-slope boundary layer. Q J R Meteorol Soc 116:637–670. doi: 10.1256/smsqj.49306

Serafin S, Zardi D (2010) Structure of the Atmospheric Boundary Layer in the Vicinity of a Developing Upslope Flow System: A Numerical Model Study. J Atmos Sci 67:1171–1185. doi: 10.1175/2009JAS3231.1

Sreenivasan KR, Antonia RA (1997) the Phenomenology of Small-Scale Turbulence. Annu Rev Fluid Mech 29:435–472. doi: 10.1146/annurev.fluid.29.1.435

Stull RB (1988) An Introduction to Boundary Layer Meteorology. Kluwe. Academic Publishe.s, Netherlands

Tatarskii VI (2005) Use of the 4/5 Kolmogorov equation for describing some characteristics of fully developed turbulence. Phys Fluids 17:03511001 – 03511012. doi: 10.1063/1.1858531

Tennekes H, Lumley JL (1972) A first course in turbulence. The MIT Press

Vitkin L, Liberzon D, Grits B, Kit E (2014) Study of in-situ calibration performance of co-located multi-sensor hot-film and sonic anemometers using a “virtual probe” algorithm. Meas Sci Technol 25:75801. doi: 10.1088/0957-0233/25/7/075801

Whiteman CD (1990) Observations of Thermally Developed Wind Systems in Mountainous Terrain. Chapter 2. In: Atmospheric Processes Over Complex Terrain. Boston, pp 5–42

Whiteman CD (2000) Mountain Meteorology: Fundamentals and Applications. Oxford University Press, New York

Wyngaard JC, Tennekes H (1970) Measurements of the small-scale structure of turbulence at moderate Reynolds numbers. Phys Fluids 13:1962–1969. doi: 10.1063/1.1693192

Zardi D, Whiteman CD (2012) Diurnal mountain wind systems. In: Mountain Weather Research and Forecasting. Berlin, pp 35–119

טורבולנציה של זרימות עולות המונעות ע״י אילוצים תרמיים

חיבור על מחקר לשם מילוי חלקי של הדרישות לקבלת התואר מגיסטר
למדעים במדעי איכות הסביבה (עם תזה)

רוני הלל

הוגש לסנט הטכניון - מכון טכנולוגי לישראל

תמוז תשע״ו, חיפה, יולי 2016

המחקר נעשה בהנחיית
פרופ׳ משנה דן ליברזון
בפקולטה להנדסה אזרחית וסביבתית

אני מודה לקרן הדו-לאומית לחינוך למדע ארה״ב-ישראל
(BSF Grant 2014075) על התמיכה הכספית הנדיבה בהשתלמותי

תקציר

זרימות מדרוניות, עולות (אנבאטיות) יורדות (קטאבאטיות), הינן נפוצות בשכבת הגבול האטמוספירית והן בעלות חשיבות עליונה להפקת תחזיות מזג אוויר מדויקות, לחקירת תהליכי השתנות האקלים, ועבור הבנה טובה יותר של הסעת מזהמים בתנאי שטח מורכבים. בפרט, חשיבות ועניין ממוקדים בנושא המיקרו-אקלים של מרכזים עירוניים אשר לעתים קרובות ממוקמים בעמקים וליד רכסי הרים. ניתן למדוד בקלות את הסקלה הגדולה של זרימה טורבולנטית בעזרת שימוש במכשור זול יחסית, אולם מכשור זה הוא בעל רמת הפרדה נמוכה במרחב ובזמן. דוגמא למכשור שכזה הינו מד רוח על קולי (סוניק). לכן הסקלות הקטנות בדרך כלל נאמדות באמצעות תאוריית ה- $-5/3$ של קולמוגורוב בשל מגבלות מדידה הכוללות בין השאר צורך בכיול חוזר של חוטי להט בתנאי שדה. זהו תהליך האורך מספר שעות וחובה לבצע אותו מחדש כאשר התנאים בשדה משתנים (כמו מהירות ממוצעת, לחות, טמפרטורה, הדרדרות איכות חוטי הלהט). יתרה מכך, תיאוריה של קולמוגורוב מותאמת לזרימות איזוטרופיות והומוגניות, אולם זרימות טורבולנטיות המונעות על ידי אילוצים תרמיים בטבע אינן תואמות לתנאים אילו ולכן התאוריה של קולמוגורוב אינה מספיקה, במיוחד לא בכדי לשמש כבסיס לאקסטרפולציה עד לסקלות הקטנות. נכון לעכשיו חסרים מודלים מקיפים כדי לתאר זרימות אנאיזוטרופיות ולא הומוגניות כפי שקיימות בטבע. המודלים צריכים לכלול מספר פרמטרים סטטיסטיים המאפיינים את הזרימה הכוללים את האנרגיה, עוצמת הטורבולנציה (TI), צידוד (skewness) של נגזרת המהירות בכיוון הזרימה הממוצע, קצב דיסיפצית אנרגיה קינטית טורבולנטית (*TKE*) ומגוון סקלות אורך כפונקציה של *Re*. סקלות אורך כוללות, בין היתר, את שלושת הסקלות שחושבו במחקר זה: סקלת האורך של קולמוגורוב (אינדיקציה של גודל הערבול בו הכוחות של הצמיגות הקינמטית דומיננטיים בהשפעתם על דיסיפצית ה-*TKE*), סקלת האורך של טיילור (אינדיקציה של גודל ערבול בו הכוחות של הצמיגות הקינמטית מתחילים להשפיע על דיסיפצית ה-*TKE*), וסקלת האורך האופקי (אינדיקציה של גודל ערבול שבו כניסת האנרגיה הקינטית מתרחשת בזרימה). בסופו של דבר דרוש תיאור מלא של התנהגות ספקטראלית (עד הסקלות הקטנות) של האנרגיה הקינטית המתבטאת על ידי התנודות בזרימה עבור שלושת רכיבי שדה המהירות. יתר על כן, תופעת פרצי הטורבולנציה הינה תופעה שקשה למדוד במיוחד בתנאי שדה טבעיים עם המכשור הנפוץ כיום, שהינו מכשור בעל רזולוציה מרחבית-זמנית נמוכה. תופעה זאת ממלאת תפקיד חשוב בייצור של זרימה טורבולנטית, ומדידתה מחייבת מכשור בעל רזולוציה גבוהה יותר.

לכן, בהתמודדות עם הצורך בקבלת נתונים בעלי דיוק גבוהה של סטטיסטיקת טורבולנציה של זרימה במדרון ומנגנוני הייצור של זרימה זו, בוצע ניסוי שדה שארך שמונה ימים בישוב נופית, הממוקם באזור הצפוני של מדינת ישראל. במהלך הניסוי בוצעו מדידות של שדה המהירות המלא ברזולוציה גבוהה. השדה התגלה כשדה בעל מחזור יומי המתאר זרימה אנבאטית המונעת מאילוצים תרמיים. המכשיר העיקרי אשר אפשר ביצוע מדידות ברמת הפרדה גבוהה הינו אנמומטר משולב המורכב מסוניק וחוטי להט מסוג hot-film (HF)–הקומבו, אשר פותח רק לאחרונה. בקומבו נעשה שימוש בנתונים האיטיים של הסוניק לכיול *אין-סיטו* של המתחים בעלי רמת הפרדה גבוהה של ה-HF על ידי שימוש ברשתות עצביות מלאכותיות (Neural Networks), מה שאפשר לבצע מדידות גם של הרכיבים הממוצעים והתונדים של שלושת רכיבי הזרימה האנבאטית במדרון. בנוסף בוצעו מדידות של תנודות הטמפרטורה בשני גבהים שונים אשר סיפקו זיהוי מצבי ריבוד, יציב/לא יציב, של מסת האוויר על המדרון. בימי המדידות לא היו מערכות סינופטיות

משמעותיות, ובמדידות היה ניתן לזהות התפתחות זרימה אנבאטית על ידי מציאת קורלציה חזקה בין שינויים במהירות הרוח הממוצעת ובשינויי הטמפרטורה היומית. ניתוח מפורט של נתונים סטטיסטיים של זרימה טורבולנטית מפותחת מסופקים במחקר זה. הם כוללים את הספקטרה שנפתרו במלואם בעבור כל שלושת הרכיבים של שדה המהירויות, מגוון סטטיסטיקות של טורבולנציה, האפיון של תופעת פרצי טורבולנציה (דהיינו סקלות אורך, תדירות התופעה, ובחינת מנגנון היצור של הפרצים), השוואה של אורכים המאפיינים את הזרימה (קולמוגורוב, טיילור, ואופקיים) בתוך דקות הכוללות פרצי טורבולנציה ועבור דקות שאינן כוללות פרצי טורבולנציה, והתאמות אמפיריות עבור מדידות עתידיות עם מכשירים ברזולוציה נמוכה ועבור מודלים נומריים.